Chemical Geology 627 (2023) 121453

Contents lists available at ScienceDirect

Chemical Geology

journal homepage: www.elsevier.com/locate/chemgeo

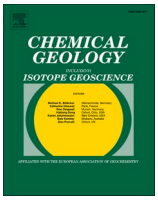

Barium isotope fractionation in barite–fluid systems at chemical equilibrium

J.T. Middleton [a,b,c,*], W.-L. Hong [d], A. Paytan [e], M.E. Auro [a,b], E.M. Griffith [f], T.J. Horner [a,b]

[a] NIRVANA Labs, Woods Hole Oceanographic Institution, Woods Hole, MA, USA
[b] Marine Chemistry & Geochemistry Department, Woods Hole Oceanographic Institution, Woods Hole, MA, USA
[c] MIT-WHOI Joint Program in Oceanography, Woods Hole, MA, USA
[d] Department of Geological Sciences, Stockholm University, Stockholm, Sweden
[e] Institute of Marine Science, University of California, Santa Cruz, CA, USA
[f] School of Earth Sciences, The Ohio State University, Columbus, OH, USA

ARTICLE INFO

Editor: Don Porcelli

Keywords:
Ion exchange
Recrystallization
Seawater
Precipitation
Dissolution
Sulfate minerals
Diagenesis

ABSTRACT

The barium isotope composition of sedimentary barite ($BaSO_4$, barium sulfate) is emerging as a powerful tracer of the sources and cycling of Ba in modern and ancient marine environments. To reliably use Ba isotopes to interrogate the marine Ba cycle, it is important to identify and constrain processes that fractionate the isotope composition of Ba in $BaSO_4$. Of particular interest is ion exchange: micro-scale dissolution and precipitation that occurs in mineral–fluid systems at chemical equilibrium. This process is often important in systems where minerals, such as $BaSO_4$, and a fluid remain in contact for prolonged periods of time; however, the impact of ion exchange on Ba isotope compositions in $BaSO_4$ is unknown. To constrain the rate and isotopic effect associated with ion exchange in $BaSO_4$–fluid systems, we conducted a series of experiments under marine-relevant conditions and interpreted the results using a multi-phase time-dependent numerical reactor model. From a series of isotope-tracer experiments, we find that $BaSO_4$–fluid ion exchange progresses at a rate between 5 and 53 pmol m^{-2} s^{-1}. In a parallel set of experiments used to assess mass-dependent isotope fractionation of Ba, the combined effect of $BaSO_4$ dissolution and precipitation while at chemical equilibrium was found to result in the continued evolution of Ba isotopes and produced a modeled offset of $\Delta^{138}Ba_{barite-dBa} = -0.10 \pm 0.05$ ‰ at isotopic equilibrium. We then constrained the magnitude of isotopic fractionation during $BaSO_4$ dissolution by fitting our data in the numerical reactor model and using previous estimates of Ba isotope fractionation during $BaSO_4$ precipitation ($\alpha_{precipitation} = 0.99968 \pm 0.00002$). At chemical equilibrium, we find our data are best explained by an $\alpha_{dissolution} = 0.99978 \pm 0.00006$, implying that $BaSO_4$ dissolution releases isotopically 'light' Ba to solution. Since the magnitude of the isotope effects associated with $BaSO_4$ precipitation and dissolution are imbalanced, ion exchange will tend to alter the isotope composition of co-located $BaSO_4$ and fluids until the two phases are offset by ≈0.10 ‰. The importance of this effect on sedimentary $BaSO_4$ likely depends on several factors and we suggest multiple site-screening criteria to maximize the utility of this emerging proxy.

1. Introduction

The geochemistry and spatiotemporal occurrence of barite (barium sulfate, $BaSO_4$) offers a window into past ocean processes on timescales spanning the Precambrian to present (e.g., Griffith and Paytan, 2012; Hanor, 2019). Micron-sized crystals of pelagic $BaSO_4$ are the dominant vector of particulate Ba in the modern ocean and are thought to precipitate in microenvironments enclosed within sinking particulate matter (e.g., Dehairs et al., 1980; Bishop, 1988). The settling of pelagic $BaSO_4$ to the sediments represents the principal sink of dissolved Ba from seawater, while the major sources of Ba to the ocean are crustal weathering (Rahman et al., 2022) and hydrothermalism (Hsieh et al., 2021; Paytan and Kastner, 1996). In marine sediments, the accumulation rate of pelagic $BaSO_4$ correlates with the downward flux of particulate organic carbon exported below the euphotic zone (Dymond et al., 1992; Eagle et al., 2003); thus, $BaSO_4$ fluxes have been used to reconstruct patterns of past export productivity (e.g., Gingele and Dahmke, 1994; Ma et al., 2014; Paytan et al., 1996a, b; Schmitz, 1987). Recent

* Corresponding author at: University of California - Santa Barbara, Santa Barbara, CA, USA.
E-mail address: jtmiddleton@ucsb.edu (J.T. Middleton).

https://doi.org/10.1016/j.chemgeo.2023.121453
Received 27 September 2022; Received in revised form 9 March 2023; Accepted 28 March 2023
Available online 31 March 2023

studies exploring the isotope composition of Ba in the marine realm demonstrated that the profile of Ba isotopes in seawater generally mirror the dissolved Ba concentration profile and range between +0.25 and +0.65 ‰ (Horner and Crockford, 2021). These profiles are thought to result from isotopic fractionation during pelagic $BaSO_4$ precipitation, which favors incorporation of isotopically 'light' Ba into the precipitated $BaSO_4$, rendering the residual Ba-depleted fluid enriched in 'heavy' Ba by a corresponding amount. The estimated magnitude of Ba isotope fractionation in the marine environment ranges between −0.35 and −0.58 ‰ (Bates et al., 2017; Bridgestock et al., 2018; Cao et al., 2020; Crockford et al., 2019; Horner et al., 2017; Horner et al., 2015; Hsieh et al., 2021; Hsieh and Henderson, 2017), leading to sedimented pelagic $BaSO_4$ with an isotopic composition between −0.2 and +0.1 ‰ (Bridgestock et al., 2018; Crockford et al., 2019). The isotope composition of Ba in $BaSO_4$ has been used to study Ba sources and environmental conditions under which $BaSO_4$ precipitation occurs (Crockford et al., 2019; Horner et al., 2017) and has been applied to reconstruct the Ba isotope composition of ancient seawater (e.g., Bridgestock et al., 2019; Hodgskiss et al., 2019). These geological applications assume—implicitly or otherwise—that $BaSO_4$ precipitation is the only process fractionating Ba isotopes during marine $BaSO_4$ formation and that the isotope composition of Ba in $BaSO_4$ is irreversibly 'locked in' after precipitation. While these assumptions may be sufficient to describe Ba isotope behavior at the environmental scale, neither assumption has been rigorously evaluated at the microscale, where processes such as ion exchange, solid state diffusion, and kinetics can influence mineral compositions.

Ion exchange is particularly relevant to $BaSO_4$–fluid systems at the microscale. Ion exchange refers to a suite of surface-mediated microscale dissolution and reprecipitation reactions that allow the mineral to exchange a portion of its atoms with ions in the surrounding fluid while at chemical equilibrium (i.e., at constant [Ba] when the fluid is saturated with respect to $BaSO_4$). Several studies showed that ion exchange affects both the chemical and isotopic composition of cations in carbonate (e.g., Chanda et al., 2019; Curti et al., 2010), oxide (Beard et al., 2010; Crosby et al., 2005) and sulfate minerals (e.g., Lestini et al., 2013), including the chemical composition of $BaSO_4$ (e.g., Bosbach et al., 2010; Curti et al., 2010). Importantly, ion exchange can occur with little or no discernible changes in mineral structure, morphology, or grain size (e.g., Gorski and Fantle, 2017) and therefore geochemical approaches are needed to study this process. Geologically speaking, ion exchange can occur rapidly; experiments conducted using a ^{133}Ba radioisotope label showed that ion exchange in certain $BaSO_4$–fluid systems can lead to complete replacement of Ba atoms in the mineral lattice of micron-sized $BaSO_4$ grains within a few thousand years (Heberling et al., 2018). Indeed, ion exchange appears to be a ubiquitous feature of $BaSO_4$–fluid systems, having now been reported across a range of ambient conditions (pH, Ba:sulfate ratio, cation substitution in the mineral, ionic strength; e.g., Bosbach et al., 2010; Curti et al., 2010; Vinograd et al., 2013; Kang et al., 2022).

Building on this progress, we undertook a systematic study to examine whether, how fast, and to what extent ion exchange affects mass-dependent Ba isotope compositions in $BaSO_4$-fluid systems under marine-like conditions. Quantifying the magnitude of these effects and the rates at which they operate is essential for understanding how the isotope composition of Ba in pelagic $BaSO_4$ is initially set and ultimately preserved. We achieved this by investigating the rate and magnitude of isotopic fractionation associated with ion exchange through a series of labeled and unlabeled laboratory experiments. We then quantified the rates and intrinsic Ba isotope effect(s) associated with ion exchange using a multi-phase, time-dependent numerical reactor model. Our multi-pronged approach illuminates the rates and magnitude of ion exchange-mediated alteration of Ba isotopes in $BaSO_4$ at chemical equilibrium. These results constrain an important aspect of the behavior of Ba isotopes in the marine environment and carry implications for the fidelity of Ba-based proxies in $BaSO_4$ in different sedimentary settings.

2. Materials, methods, and modeling

2.1. Experiment design and implementation

All sampling materials, reagents, and solution handling were conducted in accordance with trace metal clean protocols (Cutter et al., 2017). Specifically, this entailed cleaning all labware using hydrochloric and/or nitric acids, use of ultra-pure reagents (e.g., double-distilled mineral acids, high-purity reagents, 18.2 MΩ-cm-grade H_2O), and conducting all critical sample handling within laminar flow workbenches in the NIRVANA Labs metal-free workspace at the Woods Hole Oceanographic Institution (WHOI).

To begin interrogating the process of ion exchange in $BaSO_4$-fluid systems we used a simple, repeatable analogue of marine systems composed of synthetic $BaSO_4$ and artificial seawater (ASW). All experiments were seeded with 99.998 wt.% pure $BaSO_4$ (Puratronic, Alfa Aesar Lot #24177), with a nominal grain diameter of 3 μm. The synthetic $BaSO_4$ used has some differences in Sr content, morphology, and size distribution compared to pelagic $BaSO_4$, with the latter possessing higher [Sr], being more anhedral, and slightly smaller (c.f. Fig. 1; Dehairs et al., 1980).

A 25 L stock of ASW with a salinity (S) of 35 ± 0.5 was prepared following Smith and Chanley (1975) and brought to pH ≈ 8.1 by the addition of concentrated potassium hydroxide solution. The concentration of salts in the ASW is given in the Supplement. Note that the ASW stock itself contained a background of 26 ± 0.8 nmol L^{-1} Ba (±2SE, n = 5), which was present in the reagent salts. All reactions were carried out at ambient conditions (i.e., T = 20 ± 2 °C). All other experimental conditions are summarized in Table 1.

2.1.1. Isotope tracer experiments for the identification of ion exchange in marine-like systems

The rate of Ba ion exchange between $BaSO_4$ and dissolved Ba was quantified through a series of experiments whereby almost all dissolved Ba in the ASW solution was derived from dissolved ^{135}Ba, whereas solid-phase Ba in $BaSO_4$ possessed natural abundances. Dissolved ^{135}Ba was derived from a $^{135}BaCO_3$ powder (Oak Ridge National Laboratory, Lot #142890), which was dissolved in hydrochloric acid and reconstituted in ultra-high purity water for addition to experiments. Thus, if ion exchange were to occur between $BaSO_4$ and dissolved Ba, the Ba isotope ratio of the fluid, $(^{137}Ba{:}^{135}Ba)_{fluid}$, would evolve from the initial values ≈0.02 (± 1% RSD, n = 6; Table 2) toward natural abundances (i.e., $^{137}Ba{:}^{135}Ba \approx 1.7$; de Laeter et al., 2003). The amount of ^{135}Ba spike added was adjusted based on T, S, and preexisting Ba in the ASW to achieve an initial $BaSO_4$ saturation, Ω_{barite}, of 1.3:

$$\Omega_{barite} = Q/K_{sp} \quad (1)$$

where Q is the barium and sulfate ion product and K_{sp} is the apparent $BaSO_4$ solubility product. Barite saturation state was calculated using the aqueous geochemical modeling program PHREEQC (Parkhurst and Appelo, 2013). Values of Ω_{barite} >1, <1, and =1 indicate supersaturation, undersaturation, and perfect saturation, respectively. Isotope tracer experiments were initiated at slightly supersaturated conditions of Ω_{barite} = 1.3 to limit initial dissolution of $BaSO_4$. This way, any changes in $^{137}Ba{:}^{135}Ba$ should derive primarily from ion exchange and not initial dissolution of $BaSO_4$ seeds.

Experiments were carried out in duplicate in 1 L acid-washed high-density polyethylene bottles (hereafter termed 'reactors') with continuous agitation using an orbital shaker table (New Brunswick Scientific - Innova 2100). Reactors were initiated with 1 L of solution so that multiple, 2 mL-sized subsamples could be collected throughout the duration of the experiment without decreasing the volume of ASW in the reactor by >5%. Reactors were removed from the shaker table 10 min prior to sampling to allow settling of the solid phase. Isotope tracer samples were subsampled by removing an aliquot of 2 mL solution from the reaction

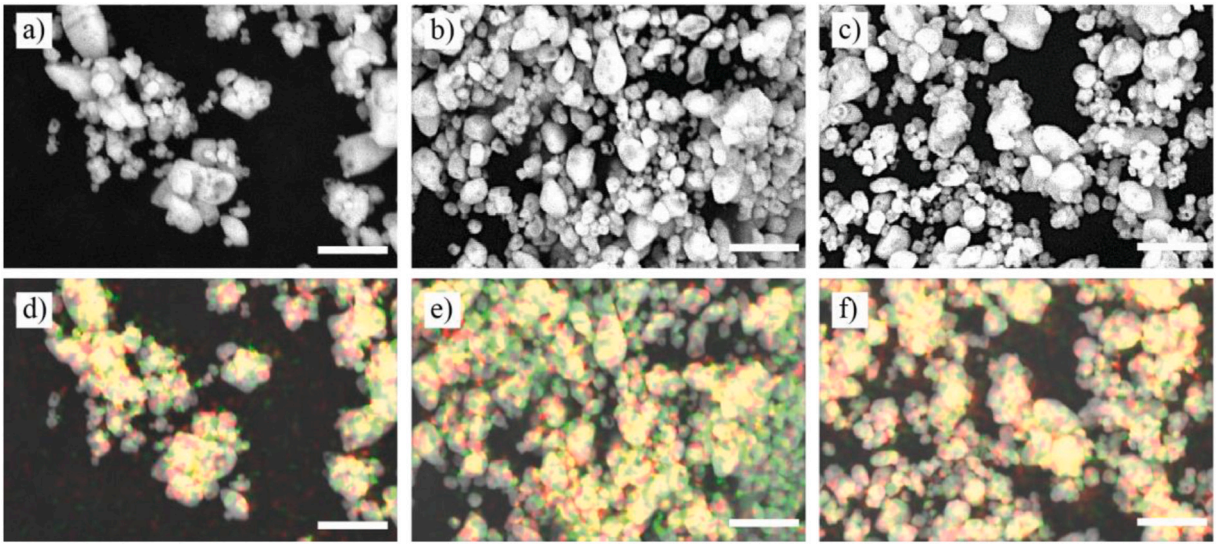

Fig. 1. SEM images of Alfa Aesar synthetic barite used in ^{135}Ba-tracer and stable isotope experiments. SEM images of the barite were taken (a) prior to experimentation and after the termination of (b) LB-135(1) and (c) HB-iso(1). The EDS spectra for barium (green) and sulfur (red) are shown in d-f. Scale bars represents 3 μm. (For interpretation of the references to colour in this figure legend, the reader is referred to the web version of this article.)

Table 1
Initial conditions for all experiments run in this study. For L_{barite}, the uncertainty is 3E-9 (± 2SE, $n = 3$).

Experiment	L_{barite}	Initial Ω_{barite}	Initial [Ba] (nM)	Initial (^{137}Ba:^{135}Ba)$_{fluid}$ (mol/mol)
HB-135(1)	0.999995	1.3	269.2	0.02
HB-135(2)	0.999995	1.3	250.8	0.02
MB-135(1)	0.99995	1.3	260.6	0.02
MB-135(2)	0.99995	1.3	260.2	0.02
LB-135(1)	0.9994	1.3	251.0	0.02
LB-135(2)	0.9994	1.3	269.3	0.02
HB-iso(1)	0.999995	0.13	26.0	
HB-iso(2)	0.999995	0.13	26.0	
MB-iso(1)	0.99995	0.13	26.0	
MB-iso(2)	0.99995	0.13	26.0	
LB-iso(1)	0.9995	0.13	26.0	
LB-iso(2)	0.9995	0.13	26.0	

vessels, immediately filtered through an acid-cleaned 0.22 μm polyethersulfone membrane disc filter, and the resultant solution collected. Aliquots were collected from reactors at the time points listed in Table 2. Oxygen was not monitored, as reactors were not inoculated and therefore oxygen drawdown was not expected.

To ensure accurate interpretation of changes in (^{137}Ba:^{135}Ba)$_{fluid}$, a control reactor was used to assess Ba adsorption onto reactor walls. This reactor was run under the same conditions as the ^{135}Ba-tracer experimental reactors, with two differences: dissolved Ba came from a $BaCl_2{\cdot}H_2O$ salt possessing natural Ba isotope ratios (Mallinckrodt Pharmaceuticals, ACS high purity grade, Lot #96847–1), and no seed $BaSO_4$ was added. Thus, [Ba] in the control reactor should depend only on adsorption. The control reactor was sampled at the initiation of the experiment and left unopened on the shaker table until it was sampled again at the completion of the experiment 180 days later.

Experiments were conducted at three different solid:fluid ratios. Hereafter we refer to the solid:fluid ratio as the leverage (L_{barite}), where L_{barite} is the proportion of Ba in the solid phase relative to the total Ba in the reactor at the start of the experiment:

$$L_{barite} = Ba_{barite} / \left(Ba_{barite} + Ba_{fluid}\right) \quad (2)$$

with all quantities are in moles. The range of initial L_{barite} tested was 0.9995, 0.99995, and 0.999995. This range was chosen as it encompasses the range of values found in pelagic sediments where Ba is routinely used in paleoceanographic reconstructions (e.g., Paytan et al., 1996a, b).

2.1.2. Assessing mass-dependent Ba isotope fractionation during ion exchange

A second set of experiments were conducted to examine if and how Ba isotopes were fractionated during ion exchange. Unlike the tracer experiments (Sec. 2.1.1.), all Ba in these experiments possessed natural abundances (i.e., without isotope tracers). This 'parallel' approach was favored over implementation of a three-isotope method (e.g., Johnson et al., 2004; Matsuhisa et al., 1978) for two related reasons. The analysis of Ba isotopes in the NIRVANA Labs is optimized for high-precision analysis of sub-5 mL seawater samples using a double spike *and* standard–sample bracketing (precision ≤ 10 ppm AMU^{-1}; (Horner et al., 2015). However, the Ba purification methods employed in this protocol are non-quantitative. Implementing a three-isotope method would require developing a new purification schema that achieved quantitative yields such that Ba isotopes could be accurately measured using only standard–sample bracketing. Though this was considered, it was ultimately deemed impractical because the magnitude of Ba isotope fractionation associated with ion exchange was predicted to be of a similar magnitude to the highest precision that can typically be achieved via standard–sample bracketing for Ba (≈35 ppm AMU^{-1}). Thus, we performed parallel experiments—a separate set of reactors run under similar conditions as the tracer experiments—that contained no spikes and could be analyzed at the highest possible precision (e.g., Johnson et al., 2004).

No additional dissolved Ba was added to the mass-dependent reactors. Thus, these reactors were initiated at $BaSO_4$-undersaturated conditions corresponding to a Ω_{barite} of 0.13 ± 0.04 (±2SE, $n = 3$), whereby initial [Ba] = 26 ± 0.8 nmol L^{-1} (±2SE, $n = 5$; Table 1). Experiments were sampled periodically until the dissolved Ba concentration in the system stabilized. Reactors were subsampled as described in Sect. 2.1.1. Following collection, the filtrate was acidified to 0.024 M HCl (pH ≤ 2) and stored for several weeks before further analysis. Aliquots were collected from the reactors at the time points listed in Table 3. The reactors were incubated for 48 to 3216 h (2 to 134 days) under constant agitation. Each experiment was performed in duplicate, with one set of experiments terminated at the midpoint to allow analysis of the solid phase.

Table 2
Experimental data from experiments evaluating the temporal evolution of (^{137}Ba:^{135}Ba)$_{fluid}$ over the course of experiments.

Experiment.sample	Time (h)	(^{137}Ba:^{135}Ba)$_{fluid}$	±2SE
HB-135(1) pre barite-addition	0.0	0.02	0.05
HB-135(1).1	0.03	0.62	0.01
HB-135(1).2	0.1	1.45	0.01
HB-135(1).3	0.2	1.54	0.01
HB-135(1).4	0.5	1.60	0.01
HB-135(1).5	1.7	1.64	0.01
HB-135(1).6	5.2	1.61	0.02
HB-135(1).7	15.9	1.64	0.02
HB-135(1).8	44.5	1.64	0.03
HB-135(1).9	144.8	1.67	0.03
HB-135(1).10	523.9	1.69	0.03
HB-135(1).11	980.6	1.67	0.03
HB-135(1).12	1315.6	1.64	0.03
HB-135(1).13	4272.0	1.66	0.02
HB-135(1) $BaSO_4$	4272.0	1.67	0.01
HB-135(2) pre barite-addition	0.0	0.02	0.05
HB-135(2).1	0.03	1.50	0.00
HB-135(2).2	0.1	1.54	0.00
HB-135(2).3	0.2	1.59	0.01
HB-135(2).4	0.5	1.59	0.01
HB-135(2).5	1.6	1.61	0.01
HB-135(2).6	5.2	1.60	0.02
HB-135(2).7	15.7	1.63	0.02
HB-135(2).8	44.5	1.65	0.02
HB-135(2).9	144.8	1.65	0.03
HB-135(2) $BaSO_4$	144.8	1.65	0.02
MB-135(1) pre barite-addition	0.0	0.02	0.05
MB-135(1).1	0.02	0.47	0.01
MB-135(1).2	0.1	0.79	0.01
MB-135(1).3	0.2	1.09	0.01
MB-135(1).4	0.5	1.26	0.01
MB-135(1).5	1.6	1.32	0.01
MB-135(1).6	5.2	1.35	0.02
MB-135(1).7	17.0	1.36	0.02
MB-135(1).8	44.5	1.44	0.02
MB-135(1).9	144.0	1.47	0.03
MB-135(1).10	524.6	1.64	0.03
MB-135(1).11	981.6	1.64	0.03
MB-135(1).12	1316.7	1.65	0.03
MB-135(1).13	4272.1	1.65	0.03
MB-135(1) $BaSO_4$	4272.1	1.67	0.02
MB-135(2) pre barite-addition	0.0	0.02	0.05
MB-135(2).1	0.02	0.18	0.01
MB-135(2).2	0.1	0.61	0.01
MB-135(2).3	0.2	0.97	0.01
MB-135(2).4	0.6	1.15	0.01
MB-135(2).5	1.7	1.27	0.01
MB-135(2).6	5.2	1.34	0.02
MB-135(2).7	16.7	1.34	0.02
MB-135(2).8	44.4	1.36	0.02
MB-135(2).9	143.8	1.44	0.03
MB-135(2) $BaSO_4$	143.8	1.66	0.01
LB-135(1) pre barite-addition	0.0	0.02	0.05
LB-135(1).1	0.03	0.04	0.03
LB-135(1).2	0.1	0.09	0.02
LB-135(1).3	0.2	0.16	0.01
LB-135(1).4	0.6	0.27	0.01
LB-135(1).5	1.6	0.35	0.01
LB-135(1).6	5.2	0.41	0.01
LB-135(1).7	17.9	0.46	0.02
LB-135(1).8	44.6	0.53	0.02
LB-135(1).9	144.7	0.68	0.02
LB-135(1).10	526.0	1.24	0.02
LB-135(1).11	982.6	1.47	0.02
LB-135(1).12	1317.7	1.57	0.03
LB-135(1).13	4272.3	1.65	0.03
LB-135(1) BaSO4	4272.3	1.65	0.02
LB-135(2) pre barite-addition	0.0	0.02	0.05
LB-135(2).1	0.0	0.07	0.02
LB-135(2).2	0.1	0.12	0.01
LB-135(2).3	0.2	0.19	0.01
LB-135(2).4	0.6	0.29	0.01
LB-135(2).5	1.6	0.39	0.01
LB-135(2).6	5.2	0.46	0.01
LB-135(2).7	17.6	0.50	0.02
LB-135(2).8	44.5	0.55	0.02
LB-135(2) BaSO4	44.5	1.64	0.02
Barite (Puratronic, Alfa Aesar Lot #24177)		1.66	0.04

2.2. Analytical methods

2.2.1. Barite dissolution

Barite samples were dissolved through an alkaline dissolution in perfluoroalkoxy alkane (PFA) vials, whereby a 1 M Na_2CO_3 solution (Puratronic, Alfa Aesar, Lot #P20E010) was added to $BaSO_4$ powder to convert samples to $BaCO_3$ (Breit et al., 1985). The amount of Na_2CO_3 added to each sample was adjusted to maintain a $BaSO_4$:Na_2CO_3 mass ratio of 1:10 and 18.2 MΩ-cm water was added to the vials such that each sample contained 10 mg of $BaSO_4$ per 2 mL of solution. Following reagent addition, samples were sonicated for 60 min at room temperature and then heated at 80 °C for ≥16 h. After cooling, the liquid containing Na_2SO_4 was decanted. To ensure the complete conversion of $BaSO_4$ to $BaCO_3$, two further rounds of Na_2CO_3 addition, sonication, heating, and decantation were carried out for all samples (as in van Zuilen et al., 2016a, 2016b). Following the third decanting, samples were rinsed with 18.2 MΩ-cm water and the remaining solid was dissolved in 2 M HCl.

2.2.2. Measurement of ^{137}Ba:^{135}Ba in isotope tracer experiments

An aliquot was subsampled from each of the filtered samples, diluted to 1900 μL with 2% HNO_3, and spiked with indium (In)—an internal standard added to all standards, samples, and blanks—to achieve a final [In] of 1 ng mL^{-1}. All samples were diluted and measured at a salinity of 1.75 to minimize non-spectral matrix effects. Filtered samples were analyzed for ^{137}Ba:^{135}Ba on a reverse quadrupole ICP-MS (iCAP-RQ, Thermo Fisher Scientific) at the WHOI Plasma Facility. Based on repeat analysis of the $BaSO_4$ samples, the precision of this measurement is estimated as 4%, relative standard deviation (RSD).

2.2.3. Measurement of mass-dependent Ba isotope variations

Non-tracer samples were prepared for Ba isotope analysis following the procedure outlined in Bates et al. (2017). Dissolved samples were equilibrated with a ^{135}Ba—^{136}Ba double spike of known concentration to achieve a spike- to sample-derived Ba concentration ratio between 1 and 2 mol/mol. Barium was pre-concentrated from 5 mL of seawater matrix through (Ba,Ca)CO_3 co-precipitation by drop-wise addition of 1 M Na_2CO_3 solution (Puratronic, Alfa Aesar). The precipitate was then dissolved in 250 μL of 2 M HCl in preparation for liquid ion-exchange chromatography. Barium was isolated by passing samples twice through 500 μL of AG 50 W-X8 (200–400 mesh) cation-exchange resin (Bio-Rad), following the purification protocol described by Horner et al. (2015). Purified Ba was analyzed for Ba isotopes using a ThermoFinnigan Neptune multi-collector inductively coupled plasma mass spectrometer (MC-ICP-MS) at the WHOI Plasma Facility. Samples were aspirated using a PFA micro-concentric nebulizer at ≈ 140 μL min^{-1}, desolvated with a CETAC Aridus II, admixed with 3–5 mL min^{-1} of N_2, and introduced into the MC-ICP-MS using an argon carrier gas. Ion currents corresponding to *m/z* 131 (Xe), 135 (Ba), 136 (Xe, Ba, Ce), 137 (Ba), 138 (Ba, La, Ce), 139 (La), and 140 (Ce) were simultaneously monitored in 30 × 4.19 s background-corrected integrations. Isotopic compositions were calculated using the three-dimensional geometric interpretation of the double-spike problem (Siebert et al., 2001) with additional processing for isobaric corrections (^{136}Xe and ^{136}Ce on ^{136}Ba,

Table 3
Experimental data from experiments evaluating the temporal evolution of δ^{138}Ba over the course of experiments.

Experiment.Sample	Time (h)	[Ba] (nM)	±2SE	δ^{138}Ba (‰)	±2SE
HB-iso(1).1	0.01	735	15	0.50	0.03
HB-iso(1).2	0.05	536	11	0.45	0.04
HB-iso(1).3	0.06	473	10	0.39	0.03
HB-iso(1).4	0.09	472	9	0.45	0.03
HB-iso(1).5	0.2	412	8	0.39	0.04
HB-iso(1).6	0.6	485	10	0.21	0.04
HB-iso(1).7	1.6	439	9	0.19	0.03
HB-iso(1).8	7.6	188	4	0.19	0.04
HB-iso(1).9	22.7	258	5	0.11	0.04
HB-iso(1).10	48.9	179	4	0.13	0.04
HB-iso(1).11	140.7	128	3	0.11	0.04
HB-iso(1).12	429.3	118	2	0.07	0.04
HB-iso(2).1	0.01	565	11	0.32	0.04
HB-iso(2).2	0.02	700	14	0.50	0.03
HB-iso(2).3	0.04	607	12	0.44	0.04
HB-iso(2).4	0.06	575	12	0.46	0.03
HB-iso(2).5	0.07	431	9	0.37	0.04
HB-iso(2).6	0.2	357	7	0.39	0.03
HB-iso(2).7	0.6	316	6	0.30	0.04
HB-iso(2).8	1.6	236	5	0.31	0.03
HB-iso(2).9	22.0	188	4	0.19	0.03
HB-iso(2).10	48.2	201	4	0.17	0.04
HB-iso(2).11	140.0	130	3	0.09	0.04
HB-iso(2) BaSO4	140.0			−0.02	0.04
MB-iso(1).1	0.01	437	9	0.33	0.03
MB-iso(1).2	0.02	316	6	0.36	0.04
MB-iso(1).3	0.04	532	11	0.32	0.03
MB-iso(1).4	0.06	475	10	0.36	0.04
MB-iso(1).5	0.07	460	9	0.37	0.04
MB-iso(1).6	0.2	386	8	0.33	0.04
MB-iso(1).7	0.6	304	6	0.33	0.04
MB-iso(1).8	2.2	253	5	0.24	0.04
MB-iso(1).9	6.3	195	4	0.24	0.04
MB-iso(1).10	21.4	162	3	0.19	0.04
MB-iso(1).11	47.6	140	3	0.14	0.04
MB-iso(1).12	139.4	136	3	0.08	0.04
MB-iso(1).13	427.9	119	2	0.08	0.05
MB-iso(1) BaSO4	427.9				
MB-iso(2).1	0.01	498	10	0.11	0.04
MB-iso(2).2	0.02	396	8	0.28	0.04
MB-iso(2).3	0.03	422	9	0.30	0.04
MB-iso(2).4	0.05	452	9	0.31	0.04
MB-iso(2).5	0.1	394	8	0.32	0.03
MB-iso(2).6	0.2	348	7	0.40	0.04
MB-iso(2).7	0.6	305	6	0.33	0.04
MB-iso(2).8	1.6	247	5	0.28	0.03
MB-iso(2).9	5.6	194	4	0.25	0.04
MB-iso(2).10	20.8	155	3	0.23	0.04
MB-iso(2).11	46.9	136	3	0.24	0.05
MB-iso(2).12	138.7	135	3	0.20	0.03
MB-iso(2) BaSO4	138.7			−0.05	0.03
LB-iso(1).1	0.01	86	2	0.15	0.04
LB-iso(1).2	0.02	143	3	0.18	0.04
LB-iso(1).3	0.03	161	3	0.24	0.03
LB-iso(1).4	0.04	177	4	0.20	0.04
LB-iso(1).5	0.1	212	4	0.14	0.03
LB-iso(1).6	0.2	246	5	0.18	0.03
LB-iso(1).7	0.6	261	5	0.20	0.03
LB-iso(1).8	1.7	230	5	0.25	0.04
LB-iso(1).9	4.4	193	4	0.25	0.05
LB-iso(1).10	21.9	164	3	0.25	0.04
LB-iso(1).11	46.7	158	3	0.19	0.06
LB-iso(1).12	335.2	119	2	0.09	0.04
LB-iso(1) BaSO4	335.2			0.02	0.03
LB-iso(2).1	0.01	100	2	0.05	0.04
LB-iso(2).2	0.02	109	2	0.08	0.04
LB-iso(2).3	0.03	129	3	0.07	0.04
LB-iso(2).4	0.04	141	3	−0.01	0.04
LB-iso(2).5	0.1	155	3	0.10	0.04
LB-iso(2).6	0.2	208	4	0.09	0.03
LB-iso(2).7	0.6	215	4	0.15	0.04
LB-iso(2).8	1.6	197	4	0.18	0.04
LB-iso(2).9	4.2	183	4	0.12	0.04
LB-iso(2).10	21.7	150	3	0.17	0.04
LB-iso(2).11	46.5	149	3	0.20	0.05
LB-iso(2) BaSO4	46.5			−0.02	0.03
Barite (Puratronic, Alfa Aesar Lot #24177)				−0.02	0.03
Initial fluid (artificial seawater)		26	0.8	0.10	0.03

^{138}Ce and ^{138}La on ^{138}Ba). Concentration- and spike-matched aliquots of NIST SRM 3104a (hereafter 'NIST') were measured after every four samples and sample Ba isotope compositions were calculated relative to the average of the nearest four measurements of the NIST standard (i.e., two ahead, two behind). Sample isotope compositions are reported as deviations in the ^{138}Ba/^{134}Ba ratio in a sample relative to the NIST, expressed in ‰:

$$\delta^{138}\mathrm{Ba} = \left[\left(^{138}\mathrm{Ba}/^{134}\mathrm{Ba}\right)_{\mathrm{sample}} \Big/ \left(^{138}\mathrm{Ba}/^{134}\mathrm{Ba}\right)_{\mathrm{NIST}} - 1\right] \times 1000 \quad (3)$$

Contributions from non-experiment-derived Ba were assessed by analyzing nine 'blanks'. Six procedural blanks constrain Ba contributions associated with sample preparation for isotope analysis and were found to range from 1168 to 2123 pg, similar to Horner et al. (2015). Dissolved concentration data are corrected for these blanks. Three chemistry-only blanks were found to range from 13 to 436 pg. The contribution of the highest blank to the sample with the lowest [Ba] was <4 %. Given the low blank contribution and poor constraints on the Ba-isotopic composition of the blank, no blank correction was applied to the Ba isotope data. Sample data uncertainties are reported as either a long-term measurement of uncertainty (±2SD about the mean; ± 0.03 ‰, Horner et al., 2015) or pooled 2SE from the replicate analyses, whichever was greater. Samples were analyzed with two, three, or four replicates depending on the concentration of Ba in the sample.

Accuracy of $BaSO_4$ and artificial seawater measurements was monitored by processing two reference materials alongside samples: NBS-127 ($BaSO_4$ powder; International Atomic Energy Agency) and SAFe D1 (GEOTRACES Northeast Pacific seawater, 1000 m). We found that NBS-127 and SAFe D1 possessed a δ^{138}Ba value of −0.29 ± 0.03 ‰ and +0.30 ± 0.04 ‰, in agreement with previous measurements of −0.29 ± 0.01 ‰ (arithmetic mean of Horner et al., 2017; Tian et al., 2019; Crockford et al., 2019) and +0.31 ± 0.03 ‰ (arithmetic mean of Hsieh and Henderson, 2017; Geyman et al., 2019; Cao et al., 2020), respectively.

2.3. Numerical time-dependent multi-phase reactor model

To quantify intrinsic reaction rates and fractionation factors from the experiments, we modeled our results using a time-dependent multi-phase reactor model developed by Sauer et al. (2021); hereafter the 'reactor model'. An overview of the reactor model assumptions, equations, implementation, and parameterization is provided in the Supplement. Briefly, the reactor model considers two processes, precipitation and dissolution of $BaSO_4$, that can affect the concentrations of the four Ba isotopes in the model (^{134}Ba, ^{135}Ba, ^{137}Ba, and ^{138}Ba). The reactor model allows simultaneous dissolution and precipitation as long as there is dissolved Ba (for precipitation) and $BaSO_4$ (for dissolution). The relative rates of the two reactions thus determine whether the overall system is more favorable for solid formation (precipitation faster than dissolution) or release of Ba to the fluid (dissolution faster than precipitation). Such a setup is consistent with ion exchange (Heberling et al., 2018; Zhen-Wu et al., 2016). Barite

precipitation is formulated as follows:

$$^{135,137,138}R_{precip.} = \left[^{135,137,138}Ba\right] \times \varphi \times \lambda_{barite,ini} \times k_{precip} \quad (4)$$

$$^{134}R_{precip.} = \left[^{134}Ba\right] \times \varphi \times \lambda_{barite,ini} \times k_{precip} \times \frac{1}{\alpha_{precip}} \quad (5)$$

where k_{precip} is the kinetic constant for precipitation of $BaSO_4$ as constrained by the overall Ba concentration in the fluid; $^{13x}R_{precip.}$ is the rate of precipitation of ^{13x}Ba; φ is the porosity (or volume ratio) of the system (Table S1). The λ_{barite} term is a formulation of the leverage in mols of Ba in $BaSO_4$:mols Ba dissolved (Eq. S9) and is recalculated at each time step in the model to account for net precipitation during the onset of the experiment. The inclusion of λ_{barite} in Eqs. (4) and (5) encodes a dependency between the kinetics of $BaSO_4$ precipitation and temporal variations in L_{barite}.

To account for the isotopic fractionation during $BaSO_4$ precipitation, the parameter $\alpha_{precip.}$ is assigned to the rate expression of $BaSO_4$ precipitation for ^{134}Ba relative to ^{138}Ba (as in Rees, 1973), where:

$$\alpha_{precip.} = \frac{k_{precip.\,138}}{k_{precip.\,134}} \quad (6)$$

The fractionation parameter is constrained by the changes of the fluid $\delta^{138}Ba$ observed in the laboratory experiments. As such, modeled rates are consistent with both the change in [Ba] and the change in $\delta^{138}Ba$ observed in experimental data.

The following rate expression is used to describe $BaSO_4$ dissolution:

$$^{135,137,138}R_{diss.} = \left(\frac{\left[Ba_{135,137,138}SO_4\right]}{MW_{135,137,138}}\right) \times (1-\varphi) \times \left(\frac{\lambda_{barite}}{\lambda_{barite,ini}}\right)^{(mrd)} \times \left(\frac{[Ba]_{eq}}{[Ba]_{ini}}\right)^{(1+mrd)} \times {}^{135,137,138}k_{diss} \quad (7)$$

$$^{134}R_{diss.} = \left(\frac{\left[Ba_{134}SO_4\right]}{MW_{134}}\right) \times (1-\varphi) \times \left(\frac{\lambda_{barite}}{\lambda_{barite,ini}}\right)^{(mrd)} \times \left(\frac{[Ba]_{eq}}{[Ba]_{ini}}\right)^{(1+mrd)} \times {}^{134}k_{diss} \times \left(\frac{1}{\alpha_{diss.}}\right) \quad (8)$$

where k_{diss} is the kinetic constant for the dissolution of $BaSO_4$ and $MW_{135,137,138}$ represents the molecular weight of the isotope of barium under consideration (i.e. 135, 137, or 138). The fit parameter *mrd,* or molar ratio dependency, determines at which concentration level the rates of precipitation and dissolution become equivalent. Model sensitivity to *mrd* is show in Fig. S3. Mass-dependent Ba isotope fractionation during dissolution is captured by $\alpha_{diss.}$, where

$$\alpha_{diss.} = \frac{^{138}k_{diss.}}{^{134}k_{diss.}} \quad (9)$$

where ^{13x}k indicates the rate constant for ^{138}Ba or ^{134}Ba. Because of the nature of our time-dependent model, the best-fit value of $\alpha_{precip.}$ depends on the choice of $\alpha_{diss.}$ Likewise, $\alpha_{diss.}$ depends on $\alpha_{precip.}$. This interdependence and the implications for assigning a unique value to either term are discussed in Sec. 4.3. Dissolution rates depend on both the changes in λ_{barite} with respect to its initial value ($\lambda_{barite}/\lambda_{barite,ini}$) and the degree of oversaturation (or undersaturation) as measured by the dissolved Ba concentration ratios between initial and chemical equilibrium states ($[Ba]_{eq}/[Ba]_{ini}$ where $[Ba]_{eq}$ = 130 nmol L^{-1} based on experimental results; Table S1).

3. Results

Representative scanning electron microscopy (SEM) images of $BaSO_4$ prior to experimentation and those recovered from reactors harvested after 46.5 (LB-ISO(2)) and 3216 h (HB-ISO(1)) are shown in Fig. 1. Only $BaSO_4$ is evident in all images, as measured by SEM with energy dispersive X-ray spectroscopy (Fig. 1 d-f). Secondary $BaSO_4$ growth would be evidenced by small $BaSO_4$ crystals on the surface of pre-existing crystals; however, at this resolution, no secondary $BaSO_4$ or growth of any other mineral is evident (Fig. 1 a-c). The lack of non-$BaSO_4$ mineral precipitation is consistent with aqueous PHREEQC geochemical modeling results (Parkhurst and Appelo, 2013), which indicated that all other Ba-containing minerals were undersaturated in the fluid throughout the experiment.

3.1. Isotope tracer experiments

The rate at which experiments achieved isotopic and chemical equilibrium was found to strongly depend on L_{barite} (Fig. 2; Table 2). All reactors used to assess ion exchange were initiated with $(^{137}Ba{:}^{135}Ba)_{fluid} = 0.02 \pm 0.05$ (±2SE, $n = 6$) and an initial $(^{137}Ba{:}^{135}Ba)_{barite} = 1.66 \pm 0.07$ (±2SE, $n = 3$). The fluid progressed from the initial $(^{137}Ba{:}^{135}Ba)_{fluid}$ toward $(^{137}Ba{:}^{135}Ba)_{barite}$ in all reactors (Fig. 2). The rate of change in $(^{137}Ba{:}^{135}Ba)_{fluid}$ shows a strong dependence on L_{barite}, with the fluids evolving faster toward solid-like $^{137}Ba{:}^{135}Ba$ at larger values of L_{barite}. Fluids in both high-leverage reactors (HB-135) reach the natural $(^{137}Ba{:}^{135}Ba)_{barite}$ ratio within 1.6 h. For the medium- (MB-135) and low-leverage (LB-135) experiments, one set of reactors was harvested before the systems achieved isotopic equilibrium so that the solids could be analyzed. The $(^{137}Ba{:}^{135}Ba)_{barite}$ of the recovered solid was identical, within uncertainty, to that of the original $BaSO_4$ powder in all reactors, consistent with the high initial leveraging (i.e., $L_{barite} \approx 1$). The other set of reactors reached $(^{137}Ba{:}^{135}Ba)_{barite}$ within 525 h (MB-135) and 4272 h (LB-135; Fig. 2; Table 2).

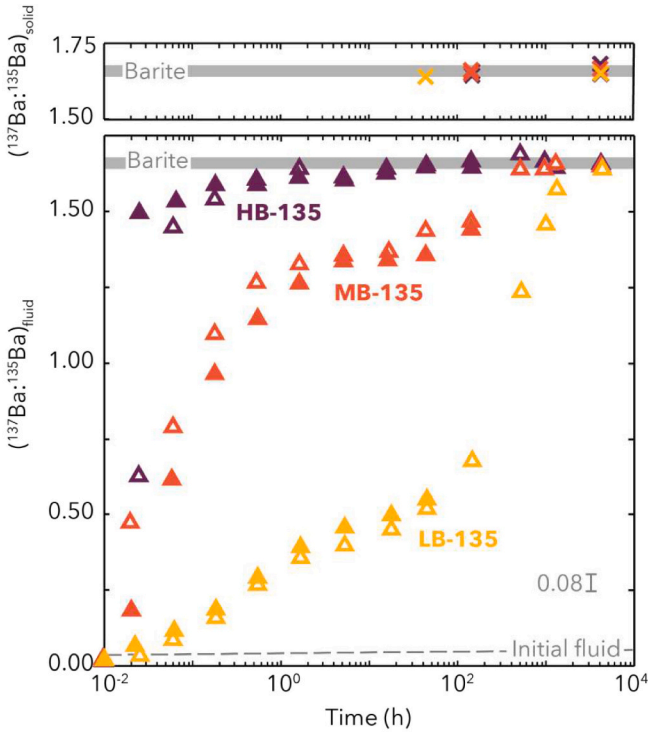

Fig. 2. Temporal evolution of tracer experiments. Initial $(^{137}Ba{:}^{135}Ba)$ of the fluid and barite are shown in grey lines, with the width of the line representing the uncertainty interval. Replicate 1 (open symbols) and replicated 2 (closed symbols) are shown for each L_{barite}. All experiments evolve from the initial ^{135}Ba-dominated composition of the fluid toward $(^{137}Ba{:}^{135}Ba)$ of the solid. Evolution of $(^{137}Ba{:}^{135}Ba)_{fluid}$ continues to progress following attainment of chemical equilibrium. Chemical equilibrium is reached after 44 h in HB-iso and MB-iso trials, and after 144 h in LB-iso(1). For clarity, $(^{137}Ba{:}^{135}Ba)_{solid}$ is plotted separately in the top panel. All solids fall within uncertainty of the initial barite.

The temporal evolution of fluid [Ba] is more difficult to assess. The proportions of ^{135}Ba and ^{137}Ba vary substantially over the course of an experiment, which precludes accurate analysis of [Ba] via an external calibration. (Precise and accurate [Ba] data are available for the mass-dependent experiments; see Sect. 3.2). In the isotope tracer experiments, we estimated dissolved [Ba] by periodically analyzing the blank-corrected ion beam intensities of ^{135}Ba, ^{136}Ba, ^{137}Ba, and ^{138}Ba in filtered solutions on the ICP-MS, as described in the Supplement (Fig. S1). Estimated [Ba] relaxes to chemical equilibrium (i.e., temporally invariant [Ba]) after 44.5 h in MB-135 and HB-135 and after 526 h in LB-135(1). Experiment LB-135(2) was harvested before chemical equilibrium was attained. In LB-135 and MB-135, estimated [Ba] approached chemical equilibrium prior to $(^{137}Ba{:}^{135}Ba)_{fluid}$ reaching $(^{137}Ba{:}^{135}Ba)_{barite}$ (Fig. 2; Fig. S1).

3.2. Mass-dependent experiments

The chemical and isotopic evolution of the mass-dependent, non-spiked reactors was also strongly dependent on initial L_{barite} (Fig. 3a-f; Table 3). Dissolved [Ba] varied significantly and systematically in all experiments. In the high-leverage (HB-ISO) and medium-leverage (MB-ISO) reactors, initial dissolution of $BaSO_4$ led to increasing [Ba] and significant oversaturation with respect to $BaSO_4$ (Fig. 3d-f). In these reactors, [Ba] increased to a maximum of 735 nmol L^{-1} ($\Omega_{barite} = 5.2$) and 532 nmol L^{-1} ($\Omega_{barite} = 3.8$) in HB-ISO and MB-ISO, respectively. In LB-ISO reactors, [Ba] increased over the first 33 min to a maximum of 260 nmol L^{-1} ($\Omega_{barite} = 1.9$) before relaxing. If assuming these initial increases in [Ba] are derived from dissolution of the $BaSO_4$ seeds, the maximum amount of $BaSO_4$ dissolution observed across all experiments was equivalent to 0.06% of the solid-phase Ba and thus has insignificant impact on the overall mass of solid barite. After initially rising, [Ba] in all experiments relaxed to a relatively stable value of 130 ± 9 nmol L^{-1} ($n = 6$, ±2SE, Table 3). Assuming mineral–fluid chemical equilibrium is achieved when Ω_{barite} is between 0.9 and 1.1 (as in Monnin et al., 1999), we calculate that dissolved [Ba] between 124 and 159 nmol L^{-1} represents chemical equilibrium. Thus, we assume that when the experiments reach and maintain [Ba] between 124 and 159 nmol L^{-1}, chemical equilibrium has been achieved.

The Ba isotope composition of the fluid was determined over the course of the experiments. In reactors with highest L_{barite}, δ^{138}Ba of the fluid in HB-ISO(1) decreased from initial values of +0.50 ± 0.03 ‰ and in HB-ISO(2) increased in the first 1.5 min, also to +0.50 ± 0.03 ‰, before decreasing. The HB-ISO replicates diverge slightly after 30 min and exhibit an average difference of +0.09 ± 0.02 ‰ ($n = 3$, ±2SE) before re-converging after 22 h. Following this, HB-ISO(1) and HB-ISO (2), approach values of +0.07 ± 0.04 ‰ and +0.09 ± 0.04 ‰, respectively (Fig. 3c). Both MB-ISO reactors showed an initial rapid increase in dissolved δ^{138}Ba to ≈ +0.4 ‰ in the first 12 min after addition of $BaSO_4$ before relaxing over the first 21 h to values of +0.19 ± 0.04 ‰ (MB-ISO (1)) and +0.23 ± 0.04 ‰ (MB-ISO(2)). During the following weeks, MB-ISO(1) continued to relax to a final value of +0.08 ± 0.05 ‰, while MB-ISO(2) relaxed to a value of +0.20 ± 0.03 ‰ before termination after 139 h for measurement of δ^{138}Ba in $BaSO_4$.

The behavior of Ba isotopes in the LB-ISO reactors is broadly similar,

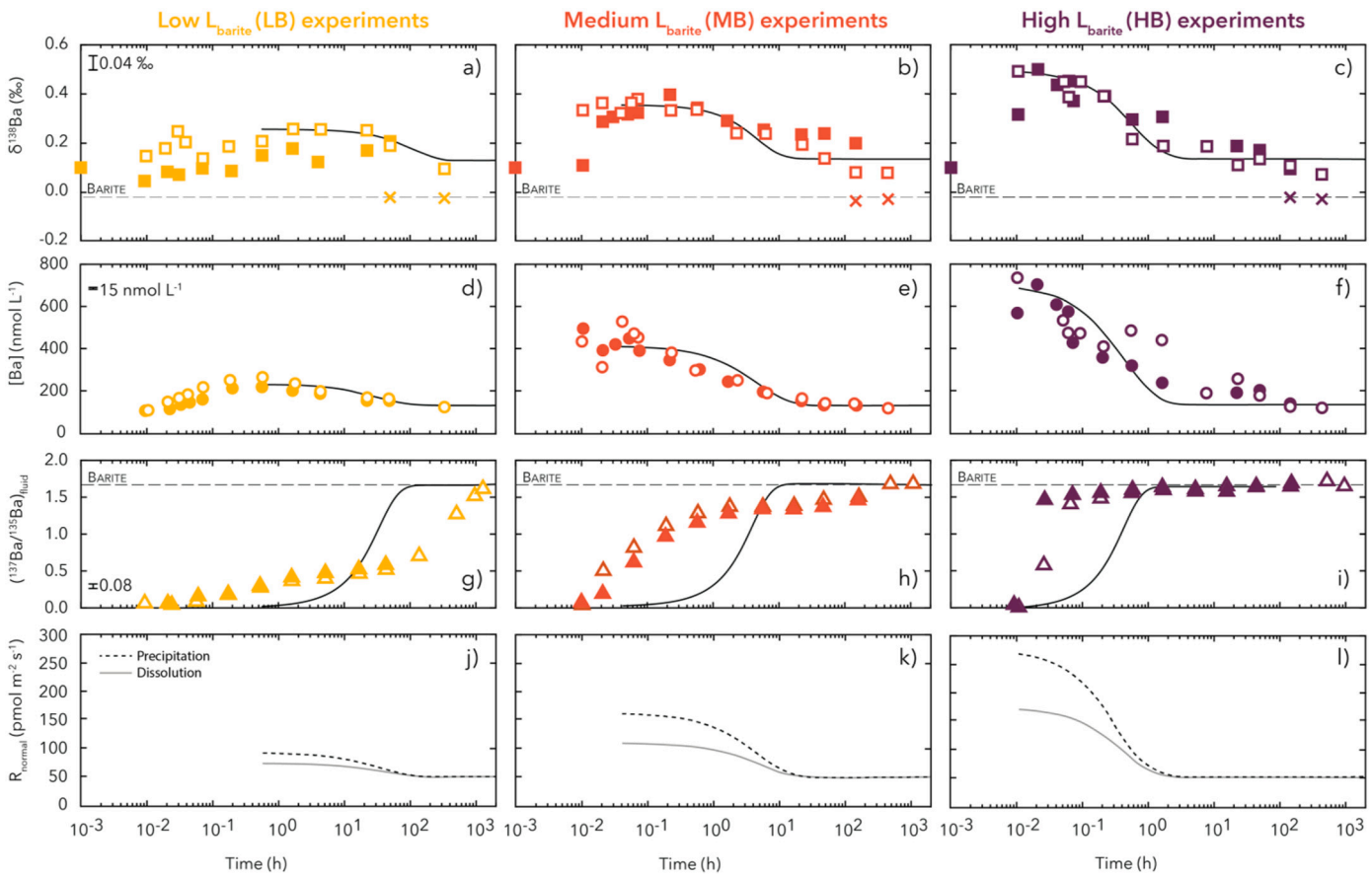

Fig. 3. Evolution of δ^{138}Ba in the fluid (squares), δ^{138}Ba of the solid (crosses), and [Ba] (circles) in mass-dependent experiments. The $(^{137}Ba{:}^{135}Ba)_{fluid}$ (triangles) in tracer experiments is reproduced from Fig. 2 for clarity. Experiments replicates are show as replicate-1 (open symbols) and -2 (filled symbols). Dashed grey lines represent the initial $BaSO_4$ value for the respective plot. The black line represents the best-fit reactor model. For the low $BaSO_4$ leverage, only LB-ISO(1) was fit to the reactor model, as LB-ISO(2) did not reach chemical equilibrium prior to termination. Panels j - l show the modeled rates of precipitation and dissolution over the course of the experiment. Ion exchange is considered to begin when the rates of precipitation and dissolution are non-zero, equal, and opposite.

Table 4
Modeled rates of ion exchange in experimental reactors. The rate of ion exchange is strongly dependent on the reactive surface area. Therefore, rates were calculated for $BaSO_4$ grains with diameters of 0.5 and 5 μm to encompass the size range of $BaSO_4$ in the synthetic barite used in experiments. $R_{apparent}$ is the bulk rate of ion exchange at chemical equilibrium (equivalent to R_{diss} and R_{precip} at chemical equilibrium), while R_{normal} is equivalent to $R_{apparent}$ normalized by the surface area of $BaSO_4$ in the reactor.

Experiment	L_{barite}	Equilibrium [Ba] (nmol L^{-1})	$R_{apparent}$ (pmol s^{-1})	R_{normal}, 0.5 μm (pmol m^{-2} s^{-1})	R_{normal}, 5 μm (pmol m^{-2} s^{-1})
HB-135	0.999995	130 ± 9	2.06E+03	5 ± 1	53 ± 1
MB-135	0.999950	120 ± 8	2.07E+04	5 ± 1	51 ± 1
LB-135	0.999503	115 ± 8	2.03E+05	5 ± 1	51 ± 1
				R_{normal} (pmol m^{-2} s^{-1})	
Curti et al. (2010)	0.990000			28 ± 16	
	0.997442			567 ± 255	
Torapava et al. (2014)	0.999978			174	
	0.999957			694	
Brandt et al. (2015)	Not reported			5	
	Not reported			4630	
Heberling et al. (2018)	Not reported			110 ± 60	
	Not reported			1400 ± 200	

although the initial 0.55 h differ from the initial changes in MB-ISO(1) and both HB-ISO reactors. In LB-ISO reactors, fluid $\delta^{138}Ba$ initially rises along with [Ba], which was also seen in MB-ISO(2), but not in MB-ISO(1) or either high-leverage experiment. After 0.55 h, dissolved [Ba] in both LB-ISO reactors begins to decrease. In LB-ISO(2), dissolved $\delta^{138}Ba$ increased to +0.2 ‰ and the reactor was harvested prior to the system reaching chemical equilibrium (Fig. 3a&d, filled symbols). In LB-ISO(1), dissolved $\delta^{138}Ba$ increases to +0.2 ‰ before decreasing to a final value of +0.09 ± 0.04 ‰ (Fig. 3a, open symbols). While the general trends between the LB-ISO duplicates are similar, the $\delta^{138}Ba$ of LB-ISO (1) was greater than those in LB-ISO(2) by +0.09 ± 0.04 ‰ on average ($n = 11$, ±2SE), with the greatest difference seen in the first 2 min following $BaSO_4$ addition. The isotopic composition of $BaSO_4$ was measured when LB-ISO(2) was terminated at 46.5 h and again at the termination of LB-ISO(1) at 427 h.

The final solid $BaSO_4$ was measured in order to calculate the isotopic offset between dissolved Ba and $BaSO_4$ in the solid after chemical equilibrium had been attained. In HB-ISO and MB-ISO, the final solid exhibited $\delta^{138}Ba$ of −0.02 ± 0.04 ‰ in HB-ISO(1) after 3216 h, −0.02 ± 0.06 ‰ in HB-ISO(2) after 140 h, −0.02 ± 0.04 ‰ in MB-ISO(1) after 428 h, and −0.05 ± 0.05 ‰ in MB-ISO(2) after 139 h. Thus, at all L_{barite}, $\delta^{138}Ba_{solid}$ remained within analytical uncertainty of the initial, unreacted $\delta^{138}Ba_{solid}$ of −0.02 ± 0.03 ‰ (Fig. 3a-c; Table 3). This implies that, despite several weeks of equilibration, the fluid in all experiments exhibited an isotopic offset from the solid while the solid itself remained unchanged within analytical uncertainty. We describe solid–fluid Ba isotopic offsets using the following notation:

$$\Delta^{138}Ba_{solid\text{–}fluid} = \delta^{138}Ba_{solid} - \delta^{138}Ba_{fluid} \quad (10)$$

where all terms have units of ‰. The final $\delta^{138}Ba$ of the solid in each experiment corresponds to $\Delta^{138}Ba_{solid\text{–}fluid}$ in the HB-ISO(1) reactor of −0.09 ± 0.06 ‰ and HB-ISO(2) by −0.12 ± 0.08 ‰. In MB-ISO(1) was offset from the solid by −0.10 ± 0.07 ‰ and MB-ISO(2) by −0.25 ± 0.06 ‰. In LB-ISO, the Ba isotope composition of $BaSO_4$ was found to be −0.02 ± 0.03 ‰ in LB-ISO(1) and −0.02 ± 0.03 ‰ in LB-ISO(2), equivalent to $\Delta^{138}Ba_{solid\text{–}fluid}$ of −0.11 ± 0.06 ‰ and −0.22 ± 0.06 ‰, respectively (Table 3). Notably, the LB-ISO(2) reactor was harvested prior to achieving chemical equilibrium (Fig. 3d) and therefore was not considered to undergo a significant period in which ion exchange dominated the system (Fig. 3j). The solid remained 'lighter' than the fluid in all experiments. For those experiments that achieved chemical equilibrium, the final $\Delta^{138}Ba_{solid\text{–}fluid}$ possesses a mean value of −0.13 ± 0.05 ‰ (±2SE, $n = 5$).

3.3. Reactor model results

Data from the experiments were evaluated in the reactor model to determine intrinsic rates and fractionation effects associated with ion exchange (Fig. 3 and Table 4). The rate of ion exchange is determined in the model as the value at which the rates of precipitation and dissolution are non-zero, equal, and opposite (Fig. 3j-l). Modeled rates were normalized to estimated $BaSO_4$ surface area (R_{normal}), assuming spherical $BaSO_4$ grains with a diameter of 0.5 μm or 5 μm. While this assumption affects the magnitude of the modeled rate of ion exchange, it does not affect comparison of R_{normal} between experiments, as the same source of $BaSO_4$ was used for all reactors. The initial values of R_{normal} were substantially different between reactors with different L_{barite}, with higher L_{barite} corresponding with faster initial R_{normal}. As the system approached chemical equilibrium, R_{normal} converged on similar values (Fig. 3j-l) given the same equilibrium concentration included in the rate expression of $BaSO_4$ dissolution ($[Ba]_{eq}$ in Eqs. 7 and 8). Rates are reported for two idealized scenarios encompassing the smallest (0.5 μm) and largest (5 μm) grain sizes observed in the synthetic $BaSO_4$ used in the experiments (Fig. 1). Modeled Ba ion exchange rates fall between a minimum of 5 pmol m^{-2} s^{-1} and a maximum of 53 pmol m^{-2} s^{-1} (Table 4).

4. Discussion

4.1. Evidence for ion exchange from isotope tracer experiments

The ^{137}Ba:^{135}Ba of the fluid undergoes dramatic changes in all tracer experiments (Fig. 2; Table 2). Across all six reactors, $(^{137}Ba{:}^{135}Ba)_{fluid}$ increased monotonically from the initial ^{135}Ba-tracer dominated value (≈0.02) toward $(^{137}Ba{:}^{135}Ba)_{barite}$ of ≈1.7. In contrast, the $(^{137}Ba{:}^{135}Ba)_{barite}$ exhibits no significant change from the initial value at either the intermediate or final time point. The lack of variation in $(^{137}Ba{:}^{135}Ba)_{barite}$ is consistent with mass-balance expectations, as the vast majority of Ba in each system was initially present in the $BaSO_4$ itself. For example, mass-balance considerations for the lowest-leveraged reactors indicate that even in the event of complete uptake of all dissolved ^{135}Ba into $BaSO_4$, $(^{137}Ba{:}^{135}Ba)_{barite}$ would change by only 0.0003, a value over 100 times smaller than the measurement uncertainty.

We interpret the observed changes in $(^{137}Ba{:}^{135}Ba)_{fluid}$ as deriving from ion exchange between solid $BaSO_4$ and dissolved Ba in solution. This interpretation is justified for two reasons. First, $BaSO_4$ dissolution

at the initiation of the experiments is insufficient to shift the $(^{137}Ba:^{135}Ba)_{fluid}$ of any reactor by >11% of the total observed change in $(^{137}Ba:^{135}Ba)_{fluid}$ and thus unable to explain the overall changes observed (see Supplement for calculations). An additional process is needed to explain the remaining >89% of observed changes in $(^{137}Ba:^{135}Ba)_{fluid}$. Second, we do not observe any significant loss of dissolved Ba to reactor walls over the course of the control experiment containing no $BaSO_4$ seeds (Fig. S2), implying that Ba losses via adsorption are insignificant. Thus, we consider our results to be strong evidence of ion exchange in a $BaSO_4$–fluid system under marine-like conditions. This finding agrees with the experimental data of Curti et al. (2010) and theoretical calculations made by Kang et al. (2022), which showed evidence for Ba(II)-$BaSO_4$ ion exchange close to chemical equilibrium under marine-relevant conditions. We now evaluate if the rate of ion exchange in our experiments aligns with previous works and offer the first evaluation of this process on the isotope composition of Ba in $BaSO_4$.

4.2. Rates of ion exchange in marine-like systems

The isotopic exchange of Ba between fluid and $BaSO_4$ and the approach to isotopic equilibrium is generally slower than the timescale required to achieve chemical equilibrium (i.e., constant [Ba]). In the isotope tracer experiments, this is evidenced by increasing $(^{137}Ba:^{135}Ba)_{fluid}$ toward $(^{137}Ba:^{135}Ba)_{barite}$ in MB-135(1), MB-135(2), and LB-135(1) long after the system had attained chemical equilibrium (Fig. 2; Fig. S1). The continued evolution of $(^{137}Ba:^{135}Ba)_{fluid}$ while at constant total dissolved [Ba] requires Ba to be incorporated into—and Ba to be released from—$BaSO_4$ in equal and opposite quantities, the hallmark of ion exchange. In HB-135 experiments, $(^{137}Ba:^{135}Ba)_{fluid}$ approached $(^{137}Ba:^{135}Ba)_{barite}$ value within the first few minutes following $BaSO_4$ addition, which was faster than the timescale required to achieve chemical equilibrium (Fig. 2; Fig. S1). The rapidity with which $(^{137}Ba:^{135}Ba)_{fluid}$ increases in HB-135 may result from the large amount of available reactive surface area. A large reactive surface area may also account for slight increases in $[Ba]_{eq}$ with increasing L_{barite}, which can arise through local disequilibrium at the solid surface allowing greater $BaSO_4$ dissolution. Analogous behavior has been described for the Ca(II)-calcite ($CaCO_3$) system by Chanda et al. (2019). Under this scenario, as L_{barite} increases, local disequilibria allow for a greater net rate of dissolution and a proportionate increase in net re-precipitation, thereby allowing the rapid changes observed in $(^{137}Ba:^{135}Ba)_{fluid}$ of HB-135(1) and HB-135(2). To fully understand the kinetics of ion exchange, we assess differences in the bulk ($R_{apparent}$) and surface-area-normalized (R_{normal}) rates using the reactor model.

We fit temporal changes in $(^{137}Ba:^{135}Ba)_{fluid}$, [Ba], and $\delta^{138}Ba$ using the reactor model (Fig. 3, solid black lines). The $(^{137}Ba:^{135}Ba)_{fluid}$ data were from the isotope tracer experiments, whereas [Ba] and $\delta^{138}Ba$ in the fluid were obtained from the mass-dependent experiments that were run in parallel. The goal of this modeling was to capture overall trends in $(^{137}Ba:^{135}Ba)_{fluid}$, [Ba], and $\delta^{138}Ba$ on a shared time axis. Therefore, we optimize the model fit for all three data types simultaneously, rather than individually. This approach leads to sub-optimal model fits in some cases, particularly for $(^{137}Ba:^{135}Ba)_{fluid}$; however, it allows for a more conservative estimate of the true rate of ion exchange as it accounts for the variation of all three data types as a result of the same process, rather than optimizing model–data fits for each data type alone.

The modeled bulk rate of ion exchange, $R_{apparent}$, for each reactor was dependent on the L_{barite} in each experiment (Table 4). When normalized to estimated $BaSO_4$ surface area, ion exchange rates converged to within one order of magnitude, falling between 5 pmol m^{-2} s^{-1} and 53 pmol m^{-2} s^{-1}. The convergence of the modeled rate when normalized to surface area is consistent with ion exchange occurring as a surface-mediated process, as reported previously by Zhen-Wu et al. (2016), Bracco et al. (2017), Heberling et al. (2018), and Vital et al. (2020). These values represent maximum rates, as ion exchange in $BaSO_4$–fluid systems slows over time (Bosbach et al., 2010; Heberling et al., 2018). Our range of rates is highly consistent with the 28 ± 16 pmol m^{-2} s^{-1} reported by Curti et al. (2010) for Ba ion exchange in $BaSO_4$–fluid systems under marine-like conditions. Other studies reported generally faster rates, ranging from 5 to 4630 pmol m^{-2} s^{-1} (Torapava et al., 2014; Brandt et al., 2015; Heberling et al., 2018), though these experiments were conducted under non-marine conditions and are thus unlikely to be directly comparable to our results.

4.3. Fractionation of barium isotopes during ion exchange

The fluid exhibits considerable variation in $\delta^{138}Ba$ over the course of an experiment, which we contend derives principally from $BaSO_4$–fluid ion exchange at chemical equilibrium. von Allmen et al. (2010) showed that $BaSO_4$ precipitated under strongly supersaturated conditions fractionates Ba isotopes with $\alpha_{precip.} = 0.99968 \pm 0.00002$ (±2SE, $n = 2$). If this were the only process occurring in our experiments, $\delta^{138}Ba_{fluid}$ would be expected to increase when dissolved [Ba] decreases. We observe the opposite trend, whereby both $\delta^{138}Ba_{fluid}$ and [Ba] decrease over time. This indicates that changes in $\delta^{138}Ba$ are unlikely to be occurring solely through a unidirectional precipitation reaction. Barium isotope behavior is instead being governed by ion exchange, as evidenced by the tracer experiments. Thus, unidirectional reactor frameworks, such as Rayleigh distillation, are not applicable to our system. We therefore use the reactor model to quantify the fractionation effects associated with ion exchange in the mass-dependent experiments. This model is preferred as it can account for concurrent isotopic fractionation during precipitation and dissolution.

The [Ba] and $\delta^{138}Ba$ of the system evolves over three periods. In the first period, at the initiation of each experiment, [Ba] and $\delta^{138}Ba$ increase. The largest increases are observed in HB-ISO experiments, with an initial increase in [Ba] and $\delta^{138}Ba$ that is likely not sufficiently resolved by the first few sampling points. In MB-ISO experiments, a similar increase in [Ba] and $\delta^{138}Ba$ was observed. The MB-ISO(2) experiment captured the increase in $\delta^{138}Ba$ over the first two time points (~1 min), concomitant with an increase in [Ba]. An initial rise in [Ba] is also seen in LB-ISO experiments, with an inflection point after 0.55 h. This first period of the system, where [Ba] initially increases, is not considered in our reactor model. This portion of the experiment, representing ≪0.1% of the total duration of any reactor equilibration experiment, likely represents a kinetically controlled reaction that occurs shortly after $BaSO_4$ seeds are added to nominally Ba-free seawater. While interesting, our focus is on the other 99.9% of the experiment, specifically how [Ba] and $\delta^{138}Ba$ evolve as the system moves toward (and achieves) chemical equilibrium.

Why [Ba] and $\delta^{138}Ba$ initially increase in our experiments is not immediately clear. We offer two possibilities. First, there may be $BaSO_4$ dissolution between the addition of the seeds and the first sampling time point. This dissolution leads to elevated [Ba], which is quickly lowered by $BaSO_4$ precipitation, leading to enrichment of ^{138}Ba in the fluid. Alternatively, it is possible that there are isotopic heterogeneities in the synthetic $BaSO_4$ used in our experiments and the first grains to dissolve were isotopically 'heavier' than those that dissolve later. Both explanations are speculative; however, it is important to keep in mind that if ion exchange is the dominant process in these systems, any initial isotope changes will be subsequently erased and the system will converge toward the same isotopic offset, regardless of L_{barite}. Similar overprinting of initial isotope compositions by ion exchange has been observed in a number of other mineral–fluid systems and these initial compositional variations were similarly argued to have no impact on the interpretation of subsequent near-equilibrium isotopic effects (e.g., Oelkers et al., 2019).

We demark the start of the second period as the point when the system switches from net dissolution to net precipitation (i.e., net removal of Ba from the aqueous to solid phase), which serves as the initial condition for our numerical model as it represents the beginning

of the relaxation toward chemical equilibrium. Throughout this period, the forward reaction (precipitation) dominates over the reverse reaction (dissolution; e.g., Oelkers et al., 2018; Oelkers and Schott, 2001; Schott et al., 2009; Schott and Oelkers, 1995), driving a decrease in dissolved [Ba].

In the third period, the system approaches and maintains chemical equilibrium, at which point the relative rates of precipitation and dissolution are balanced. The third period can be seen when the modeled precipitation and dissolution rates are equivalent (Fig. 3j-l). During the chemical equilibrium period, δ^{138}Ba of the fluid continued to evolve before attaining a relatively stable offset from the solid of $\Delta^{138}Ba_{solid-fluid} = -0.13 \pm 0.05$ ‰ (±2SE, $n = 5$). We contend that the continued evolution of δ^{138}Ba while at chemical equilibrium is a consequence of the coinciding processes of precipitation and dissolution—that is, ion exchange—dominating the temporal evolution of dissolved δ^{138}Ba. The behavior observed in our experiments is conceptually similar to that of dynamic equilibrium (e.g., Oelkers et al., 2018), whereby the isotopic composition of the system can evolve even after chemical equilibrium has been achieved. Such variations are consistent with the calculations of Druhan et al. (2013) and Steefel et al. (2014), which predict continued isotopic equilibration of a mineral-fluid system while at chemical equilibrium.

The solid–fluid offset at isotopic equilibrium, $\Delta^{138}Ba_{barite-dBa}$, can be used to place constraints on the magnitude of the intrinsic Ba isotope effects of $BaSO_4$ precipitation and dissolution, $\alpha_{precip.}$ and $\alpha_{diss.}$, respectively. As noted above, the reactor model was optimized to fit [Ba], δ^{138}Ba, and (^{137}Ba:^{135}Ba)$_{fluid}$ data from the tracer experiments. In doing so, both the rate of reaction and the magnitudes of fractionation were calculated simultaneously. Modeled $\Delta^{138}Ba_{barite-dBa}$ after the system has reached isotopic equilibrium represents the combined net effect of the forward reaction (precipitation) and the back reaction (dissolution) at chemical equilibrium and was found to have a magnitude of $\Delta^{138}Ba_{barite-dBa}$, $= -0.10 \pm 0.05$ ‰. As such, the model can only offer a non-unique solution for $\alpha_{precip.}$ and $\alpha_{diss.}$; there is a continuum of fractionation factors that are consistent with our results (Fig. 4). However, it is possible to assign a unique value of $\alpha_{diss.}$ if we assign a value of $\alpha_{precip.}$

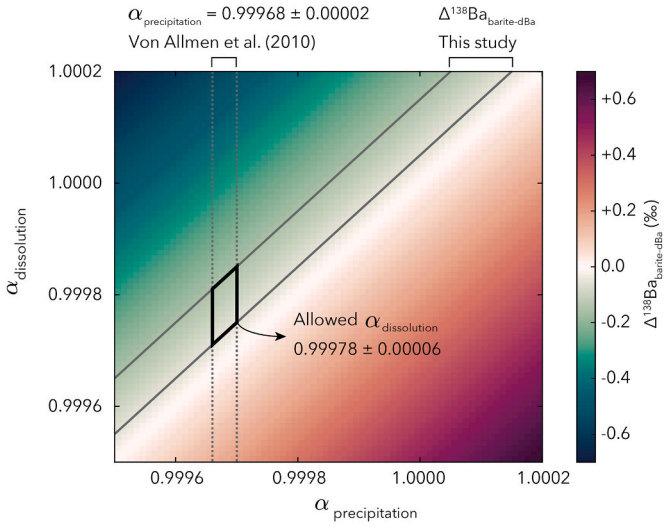

Fig. 4. Heat map of the offset between Ba isotopes in $BaSO_4$ and dissolve Ba(II) ($\Delta^{138}Ba_{barite-dBa}$) at isotopic equilibrium produced by different combinations of the fractionation factors for precipitation ($\alpha_{precip.}$) and dissolution ($\alpha_{diss.}$). Von Allmen et al. (2010) constrain the isotopic fractionation of Ba during $BaSO_4$ precipitation as $\alpha_{precip.} = 0.99968 \pm 0.00002$, shown by the dotted grey lines. Solid grey lines show the modeled offset between $BaSO_4$ and the fluid at isotopic equilibrium, where $\Delta^{138}Ba_{barite-dBa} = -0.10 \pm 0.05$ ‰. Given these constraints, the area encompassed by the bold quadrangle represents the possible range of $\alpha_{diss.}$. The average allowable $\alpha_{diss.}$ is 0.99978 ± 0.00006, with release of isotopically 'light' Ba to solution.

The most robust estimate for $\alpha_{precip.}$ is 0.99968 ± 0.00002 (±2SE, n = 2), obtained by von Allmen et al. (2010), later confirmed by Böttcher et al. (2018), and further validated here by our preliminary experiments examining $BaSO_4$ precipitation (see the Supplement). Using $\alpha_{precip.}$ =0.99968 ± 0.00002, the best-fit $\alpha_{diss.}$ is calculated as 0.99978 ± 0.00006, indicating the release of 'light' Ba to solution during $BaSO_4$ dissolution under marine-like conditions (Fig. 4). This finding broadens the characterization of Ba isotope fractionation during $BaSO_4$ dissolution, which had previously been studied solely in the context of proton-promoted dissolution (Böttcher et al., 2018; von Allmen et al., 2010) and carbonate replacement of the sulfate group (van Zuilen et al., 2016b) and found to be non-fractionating in both cases.

We speculate that the process driving release of 'light' Ba isotopes during dissolution modeled here may be attributed to the tendency for 'lighter' ^{134}Ba—O bonds to break relatively easier compared to stronger ^{138}Ba—O bonds in the $BaSO_4$ structure (see, e.g., Criss, 1999; Hoefs, 2009). Similar release of the 'light' metal isotopes to the fluid during dissolution has been observed in carbonate and silicate minerals (Maher et al., 2016; Oelkers et al., 2018; Oelkers et al., 2015). This is consistent with studies showing that the magnitude of isotope fractionation during dissolution is strongly dependent on dissolution mechanism (e.g. Kiczka et al., 2010; Li et al., 2021; Skulan et al., 2002; Wiederhold et al., 2006). While proton-promoted dissolution is generally non-fractionating for a variety of minerals, other mechanisms of dissolution can produce measurable isotope effects (e.g., Kiczka et al., 2010; Skulan et al., 2002; Wiederhold et al., 2006).

4.4. Implications for the fidelity of barium isotopes in marine barite

Our results show that ion exchange occurs rapidly in $BaSO_4$–fluid systems at salinity, temperature, [Ba], $BaSO_4$ crystal size, and L_{barite} relevant to the marine environment. Modeled rates of ion exchange were between 5 and 53 pmol m^{-2} s^{-1} over the time period studied. These findings add to a growing body of evidence indicating that ion exchange affects Ba cycling under conditions ranging from open marine to industrial settings (e.g., Bosbach et al., 2010; Curti et al., 2010; Vinograd et al., 2013; Torapava et al., 2014; Brandt et al., 2015; Heberling et al., 2018). Ion exchange in $BaSO_4$-fluid systems has been shown to penetrate beyond the surface layer and into the crystal lattice (Curti et al., 2010; Brandt et al., 2015; Heberling et al., 2018). Critically, our experiments illustrate that ion exchange allows the Ba isotope composition of dissolved Ba, and therefore $BaSO_4$ (even if these changes in the solid phase are not always detected), to continue to evolve toward isotopic equilibrium even after chemical equilibrium has been achieved. This process leads to a modeled characteristic offset of $\Delta^{138}Ba_{barite-dBa}$, of $= -0.10 \pm 0.05$ ‰, which represents the final offset in δ^{138}Ba between $BaSO_4$ and dissolved Ba when isotopic equilibrium has been reached. We contend that this offset arises through coupled precipitation and dissolution at chemical equilibrium, that is, ion exchange. Assuming neither $\alpha_{diss.}$ or α_{precip} are affected by pressure, ion exchange may also affect the isotope composition of Ba in $BaSO_4$ deposited in pelagic sediments, though the temperature, pH, and alkalinity dependence of these values requires further study. Additionally, variability in the composition of pelagic $BaSO_4$, such as chemical heterogeneities, may affect the rate of precipitation and dissolution and likewise requires additional constraints. Since $BaSO_4$ may be in contact with porewaters for months to many thousands of years, ion exchange is likely to be important in sedimentary systems. This has several implications for the isotopic composition of Ba in fluids and $BaSO_4$ in the marine environment.

The importance of ion exchange to the Ba isotope composition of $BaSO_4$ depends strongly on the L_{barite} of the system. That is, while ion exchange will push $BaSO_4$–fluid systems toward an isotopic equilibrium whereby $\Delta^{138}Ba_{barite-dBa} = -0.10 \pm 0.05$ ‰, the proportion of Ba initially in $BaSO_4$ impacts whether this change will measureably alter the initial δ^{138}Ba of $BaSO_4$. For example, if dissolved Ba and $BaSO_4$ both have an initial composition of δ^{138}Ba = 0.00 ‰ and ion exchange

progresses until isotopic equilibrium is achieved, a system with $L_{barite} = 0.5$ will have a final dissolved composition of $\delta^{138}Ba = +0.05$ ‰ and a final $BaSO_4$ composition of $\delta^{138}Ba = -0.05$ ‰. Comparatively, in a system more like those routinely used for paleoceanographic reconstructions with $L_{barite} \approx 1$ (e.g., Paytan and Kastner, 1996), the situation is different; $BaSO_4$ will not measurably change from the initial value of $\delta^{138}Ba = 0.00$ ‰, whereas the fluid will evolve to $\delta^{138}Ba \approx +0.10$ ‰. Assuming that our results can be translated to marine sediments, similar offsets should be observed between pore fluids and co-located $BaSO_4$ in systems that are at isotopic equilibrium. Ion exchange will have the most impact on the $\delta^{138}Ba$ of $BaSO_4$ in systems with low L_{barite}.

Environmental factors, in addition to the system leverage, may also be important in regulating ion exchange and Ba isotope composition of $BaSO_4$ in marine systems. In sediments, L_{barite} is controlled both by the concentration of Ba in the fluid, the abundance of $BaSO_4$, and the delivery of dissolved Ba to the fluid phase. Marine pore fluids may experience diffusive fluxes (McManus et al., 1998), hydrothermal (Snelgrove and Forster, 1996) or cold seep circulation (Hu et al., 2019; Rooze et al., 2020), and submarine groundwater discharge (Hong et al., 2019), which could affect the amount and rate of turnover of the dissolved Ba pool. Both diffusive fluxes and active flows through pore fluids have the potential to supply 'new' dissolved Ba to $BaSO_4$ surfaces, effectively lowering L_{barite}, and therefore may impact the $\delta^{138}Ba$ of $BaSO_4$—even in systems with high apparent L_{barite}. Available reactive surface area likely also impacts ion exchange, which may be decreased by organic or mineral coatings in marine settings.

The degree to which ion exchange can penetrate the interior of a $BaSO_4$ crystal may also depend on the presence of other elements, such as radium (Ra), Sr, and Ca. Higher Ra contents in the $BaSO_4$ crystal lattice generally leads to more ideal solid solution behavior, and therefore interior ions can more easily exchange with surrounding fluids (Curti et al., 2010). In addition to the effect of Ra content on the exchangeability of Ba, Ra contained within $BaSO_4$ is commonly used to reconstruct sediment age models (Paytan et al., 1996a, b), and is also known to undergo Ra(II)-$BaSO_4$ ion exchange (Curti et al., 2010). Like Ra, Sr forms an ideal solid solution with $BaSO_4$ (e.g., Hanor, 2019) and the isotope composition of Sr is routinely measured in $BaSO_4$ (e.g., Paytan et al., 1993; Paytan et al., 2021). The effect of Sr on rates of Ba ion exchange—and of ambient [Sr] on Sr isotope exchange—deserve additional study, although current data of radiogenic Sr isotope ratios in $BaSO_4$ used for paleoceanographic applications suggest that impacts on the $BaSO_4$ values are below detection limits (Paytan et al., 1993). Likewise, Ca is another minor element whose marine isotope composition has been reconstructed using $BaSO_4$ (e.g., Griffith et al., 2008). Though Ca forms a non-ideal solid-solution with $BaSO_4$ (Hanor, 2019), there is evidence of Ca ion exchange in calcium sulfate minerals (e.g., Harouaka et al., 2019) and thus this process may also be important in $BaSO_4$. As with $\delta^{138}Ba$, the degree of ion-exchange-mediated alteration of Ra, Sr, and Ca will be sensitive to the leverage (i.e., the amount of the given element in $BaSO_4$ compared to that in the fluid), the presence of other solid phases in the sediment and their susceptibility to ion exchange, and the degree of isotopic disequilibrium between $BaSO_4$ and the fluid. To further understand the role of ion exchange in $BaSO_4$, we suggest future studies addressing the interaction of Ra, Sr, Ca, $BaSO_4$, and the permeation of isotopic signatures imparted by ion exchange into the interior of $BaSO_4$ crystals. In environmental settings, the degree of alteration of $\delta^{138}Ba$ in sedimented $BaSO_4$ may be impacted by any number of these effects and these represent important areas for further study.

The results reported in this study illustrate that Ba isotope compositions in $BaSO_4$-fluid systems can evolve toward isotopic equilibrium after chemical equilibrium has been reached. These results are coherent with similar observations reported for other sulfate minerals, including Mg isotopic fractionation in epsomite (Li et al., 2011) and Ca isotopic fractionation in gypsum (Harouaka et al., 2019). Similar observations have also been reported for Ca isotopes in carbonates (Chanda et al., 2019; Fantle and DePaolo, 2007), potassium isotopes in a variety of K-salts (Li et al., 2017), and magnesium isotopes in magnesite and hydromagnesite (Oelkers et al., 2018; Pearce et al., 2012). These studies indicate that isotope compositions continue to progress toward isotopic equilibrium after chemical equilibrium has been attained. Our study shows that similar processes affect Ba isotopes in $BaSO_4$-fluid systems, at least for synthetic barites and artificial seawater. Assuming that similar processes affect natural barites in the ocean, our results show that ion-exchange-mediated alteration of Ba isotopes can lead to isotope variations of up to -0.10 ± 0.05 ‰ in $BaSO_4$.These findings are important to consider when interpreting the Ba isotope composition of ancient $BaSO_4$, as this range of variation is of a similar magnitude to variations in $\delta^{138}Ba$ seen in the geological record ($\pm$ 0.1 ‰; e.g., Bridgestock et al., 2019). Thus, to reliably interpret sedimentary Ba isotope variations as reflecting changes in marine biogeochemistry and not ion exchange, it will be important to have some confidence that sites have retained high L_{barite} over their history.

Careful selection of study sites that are thought to have maintained high L_{barite} will ameliorate the potential confounding effects of ion exchange on the isotopic composition of $BaSO_4$ and thereby allow accurate interpretation of $\delta^{138}Ba$. Generally, areas with high export productivity impart sediments with significantly more $BaSO_4$ than other regions (Paytan and Kastner, 1996; Eagle et al., 2003; Bridgestock et al., 2018), aiding in the maintenance of a high L_{barite}. However, care must be taken in areas of very high organic matter export, which may ultimately lead to the development of sulfidic conditions in porewaters in which $BaSO_4$ will undergo net dissolution, thereby decreasing L_{barite}. Based on our findings, we suggest that well-oxygenated sites with high L_{barite} and minimal resupply of new dissolved Ba to the pore fluids are the most likely environments for sedimented $BaSO_4$ to retain primary compositional information. This may be tested by examining $BaSO_4$ and co-located pore waters and will be critical for establishing the optimal conditions for preserving the primary $\delta^{138}Ba$ in marine $BaSO_4$ over geological timescales.

5. Conclusions

The results described here provide evidence of ion exchange and the co-evolution of mineral isotopic signatures toward isotopic equilibrium in $BaSO_4$-fluid systems at chemical equilibrium under marine-like conditions. This alteration is thought to progress through micro-scale dissolution and reprecipitation reactions. We find that Ba ion exchange in $BaSO_4$–fluid systems occurs at rates between of 5–53 pmol Ba m^{-2} s^{-1}. Using a value of $\alpha_{precip.}$ from the literature (0.99968 ± 0.00002), we find that our data are best explained if $BaSO_4$ dissolution also occurs with a small fractionation, equivalent to $\alpha_{diss} = 0.99978 \pm 0.00006$ (i.e., preferential release of isotopically light Ba). Since the isotope effects of precipitation and dissolution are unequal, equilibrium between $BaSO_4$ and fluids is expected to result in $\Delta^{138}Ba_{barite-dBa} = -0.10 \pm 0.05$ ‰ at isotopic equilibrium, which several of our experiments approach. Alteration of Ba isotope compositions through this process can occur without any clear visual evidence of mineral alteration. This suggests that the primary isotopic composition of Ba in geologic $BaSO_4$ may be altered by ion-exchange. The degree to which the primary Ba isotope signature is altered in $BaSO_4$ will depend on L_{barite}, the initial isotopic disequilibrium, the reactivity of environmental $BaSO_4$, and the supply of new dissolved Ba to pore fluids. Each of these areas requires additional study and will provide important constraints on how best to apply $\delta^{138}Ba$ in $BaSO_4$.

Declaration of Competing Interest

The authors declare that they have no known competing financial interests or personal relationships that could have appeared to influence the work reported in this paper.

Data availability

All data appear within the tables of the article and Supplement.

Acknowledgments

Thanks to Peter Crockford and Sune Nielsen for illuminating discussions, Gretchen Swarr and Jerzy Blusztajn for assistance in the WHOI Plasma Facility, and to Christopher Kinsley for insightful feedback. We acknowledge financial support from the Ocean Vision 2030 Fund and its generous donors through the Woods Hole Oceanographic Institution, as well as the National Science Foundation, which provided a Graduate Research Fellowship to J.T.M. and grants to T.J.H. (OCE-1827401 & OCE-2023456), A.P. (OCE-1827431), and E.M.G. (EAR-1053312).

Appendix A. Supplementary data

Supplementary data to this article can be found online at https://doi.org/10.1016/j.chemgeo.2023.121453.

References

Bates, S.L., Hendry, K.R., Pryer, H., Kinsley, C.W., Pyle, K.M., Woodward, E.M.S., Horner, T.J., 2017. Barium isotopes reveal role of ocean circulation on barium cycling in the Atlantic. Geochim. Cosmochim. Acta 204, 286–299. https://doi.org/10.1016/j.gca.2017.01.043.

Beard, B.L., Handler, R.M., Scherer, M.M., Wu, L., Czaja, A.D., Heimann, A., Johnson, C. M., 2010. Iron isotope fractionation between aqueous ferrous iron and goethite. Earth Planet. Sci. Lett. 295, 241–250. https://doi.org/10.1016/j.epsl.2010.04.006.

Bishop, J.K.B., 1988. The barite-opal-organic carbon association in oceanic particulate matter. Nature 332, 341–343.

Bosbach, D., Böttle, M., Metz Karlsruher, V., 2010. Experimental Study on Ra^{2+} Uptake by Barite ($BaSO_4$). Stockholm, Sweden.

Böttcher, M.E., Neubert, N., von Allmen, K., Samankassou, E., Nägler, T.F., 2018. Barium isotope fractionation during the experimental transformation of aragonite to witherite and of gypsum to barite, and the effect of ion (de)solvation. Isot. Environ. Health Stud. 54, 324–335. https://doi.org/10.1080/10256016.2018.1430692.

Bracco, J.N., Lee, S.S., Stubbs, J.E., Eng, P.J., Heberling, F., Fenter, P., Stack, A.G., 2017. Hydration Structure of the Barite (001)-Water Interface: Comparison of X-ray Reflectivity with Molecular Dynamics Simulations. J. Phys. Chem. C 121, 12236–12248. https://doi.org/10.1021/acs.jpcc.7b02943.

Brandt, F., Curti, E., Klinkenberg, M., Rozov, K., Bosbach, D., 2015. Replacement of barite by a (Ba,Ra)SO_4 solid solution at close-to-equilibrium conditions: A combined experimental and theoretical study. Geochim. Cosmochim. Acta 155, 1–15. https://doi.org/10.1016/j.gca.2015.01.016.

Breit, G.N., Simmons, E.C., Goldhaber, M.B., 1985. Dissolution of barite for the analysis of strontium isotopes andother chemical and isotopic variations using aqueous sodium carbonate. Chem. Geol. 52, 333–336.

Bridgestock, L., Hsieh, Y., Porcelli, D., Homoky, W.B., Bryan, A., Henderson, G.M., 2018. Controls on the barium isotope compositions of marine sediments. Earth Planet. Sci. Lett. 481, 101–110. https://doi.org/10.1016/j.epsl.2017.10.019.

Bridgestock, L., Hsieh, Y., Porcelli, D., Henderson, G.M., 2019. Increased export production during recovery from the Paleocene–Eocene thermal maximum constrained by sedimentary Ba isotopes. Earth Planet. Sci. Lett. 510, 53–63. https://doi.org/10.1016/j.epsl.2018.12.036.

Cao, Z., Li, Y., Rao, X., Yu, Y., Hathorne, E.C., Siebert, C., Dai, M., Frank, M., 2020. Constraining barium isotope fractionation in the upper water column of the South China Sea. Geochim. Cosmochim. Acta 288, 120–137. https://doi.org/10.1016/j.gca.2020.08.008.

Chanda, P., Gorski, C.A., Oakes, R.L., Fantle, M.S., 2019. Low temperature stable mineral recrystallization of foraminiferal tests and implications for the fidelity of geochemical proxies. Earth Planet. Sci. Lett. 506, 428–440. https://doi.org/10.1016/j.epsl.2018.11.011.

Criss, R.E., 1999. Principles of Stable Isotope Distribution. Oxford University Press.

Crockford, P.W., Wing, B.A., Paytan, A., Hodgskiss, M.S.W., Mayfield, K.K., Hayles, J.A., Middleton, J.E., Ahm, A.S.C., Johnston, D.T., Caxito, F., Uhlein, G., Halverson, G.P., Eickmann, B., Torres, M., Horner, T.J., 2019. Barium-isotopic constraints on the origin of post-Marinoan barites. Earth Planet. Sci. Lett. 519, 234–244. https://doi.org/10.1016/j.epsl.2019.05.018.

Crosby, H.A., Johnson, C.M., Roden, E.E., Beard, B.L., 2005. Coupled Fe(II)-Fe(III) electron and atom exchange as a mechanism for Fe isotope fractionation during dissimilatory iron oxide reduction. Environ. Sci. Technol. 39, 6698–6704. https://doi.org/10.1021/es0505346.

Curti, E., Fujiwara, K., Iijima, K., Tits, J., Cuesta, C., Kitamura, A., Glaus, M.A., Müller, W., 2010. Radium uptake during barite recrystallization at 23±2°C as a function of solution composition: an experimental ^{133}Ba and ^{226}Ra tracer study. Geochim. Cosmochim. Acta 74, 3553–3570. https://doi.org/10.1016/j.gca.2010.03.018.

Cutter, G., Casciotti, K., Croot, P., Geibert, W., Heimbürger, L.-E., Lohan, M., Planquette, H., van de Flierdt, T., 2017. Sampling and Sample-handling Protocols for GEOTRACES Cruises. Version 3, August 2017. Toulouse, France.

de Laeter, J.R., Böhlke, J.K., de Bievre, P., Hidaka, H., Peiser, H.S., Rosman, K.J.R., Taylor, P.D.P., 2003. Atomoic Weights of the elements (IUPAC Review). Pure Appl. Chem. 75, 683–800.

Dehairs, F., Chesselet, R., Jedwab, J., 1980. Discrete suspended particles of barite and the barium cycle in the open ocean. Earth Planet. Sci. Lett. 49, 528–550.

Druhan, J.L., Steefel, C.I., Williams, K.H., DePaolo, D.J., 2013. Calcium isotope fractionation in groundwater: Molecular scale processes influencing field scale behavior. Geochim. Cosmochim. Acta 119, 93–116. https://doi.org/10.1016/j.gca.2013.05.022.

Dymond, J., Lyle, M., York, N., 1992. Barium in deep-sea sediment: a geochemical proxy for paleoproductivity. Paleoceanography 7, 163–181.

Eagle, M., Paytan, A., Arrigo, K.R., van Dijken, G., Murray, R.W., 2003. A comparison between excess barium and barite as indicators of carbon export. Paleoceanography 18. https://doi.org/10.1029/2002pa000793.

Fantle, M.S., DePaolo, D.J., 2007. Ca isotopes in carbonate sediment and pore fluid from ODP Site 807A: the Ca^{2+}(aq)-calcite equilibrium fractionation factor and calcite recrystallization rates in Pleistocene sediments. Geochim. Cosmochim. Acta 71, 2524–2546. https://doi.org/10.1016/j.gca.2007.03.006.

Geyman, B.M., Ptacek, J.L., LaVigne, M., Horner, T.J., 2019. Barium in deep-sea bamboo corals: phase associations, barium stable isotopes, & prospects for paleoceanography. Earth Planet. Sci. Lett. 525 https://doi.org/10.1016/j.epsl.2019.115751.

Gingele, F., Dahmke, A., 1994. Discrete barite particles and barium as tracers of paleoproductivity in South Atlantic sediments. Paleoceanography 9 (1), 151–168.

Gorski, C.A., Fantle, M.S., 2017. Stable mineral recrystallization in low temperature aqueous systems: a critical review. Geochim. Cosmochim. Acta 198, 439–465. https://doi.org/10.1016/j.gca.2016.11.013.

Griffith, E.M., Paytan, A., 2012. Barite in the ocean - occurrence, geochemistry and palaeoceanographic applications. Sedimentology 59, 1817–1835. https://doi.org/10.1111/j.1365-3091.2012.01327.x.

Griffith, E.M., Paytan, A., Caldeira, K., Bullen, T.D., Thomas, E., 2008. A dynamic marine calcium cycle during the past 28 million years. Science 322 (5908), 1671–1674. https://doi.org/10.1126/science.1057886.

Hanor, J.S., 2019. Barite-celestine geochemistry and environments of formation. In: Sulfate Minerals: Crystallography, Geochemistry, and Environmental Significance. Walter de Gruyter GmbH, pp. 193–275. https://doi.org/10.2138/rmg.2000.40.4.

Harouaka, K., Gorski, C.A., Fantle, M.S., 2019. Quantifying Ca exchange in gypsum using a ^{45}Ca tracer: Implications for interpreting Ca isotopic effects in experimental and natural systems. Geochim. Cosmochim. Acta 259, 371–390. https://doi.org/10.1016/j.gca.2019.05.007.

Heberling, F., Metz, V., Böttle, M., Curti, E., Geckeis, H., 2018. Barite recrystallization in the presence of ^{226}Ra and ^{133}Ba. Geochim. Cosmochim. Acta 232, 124–139. https://doi.org/10.1016/j.gca.2018.04.007.

Hodgskiss, M.S.W., Crockford, P.W., Peng, Y., Wing, B.A., Horner, T.J., 2019. A productivity collapse to end Earth's Great Oxidation. Proc. Natl. Acad. Sci. U. S. A. 116, 17207–17212. https://doi.org/10.1073/pnas.1900325116.

Hoefs, J., 2009. Stable Isotope Geochemistry, Sixth. ed. Springer-Verlag, Berlin.

Hong, W.L., Lepland, A., Himmler, T., Kim, J.H., Chand, S., Sahy, D., Solomon, E.A., Rae, J.W.B., Martma, T., Nam, S., Knies, J., 2019. Discharge of Meteoric Water in the Eastern Norwegian Sea since the Last Glacial Period. Geophys. Res. Lett. 46, 8194–8204. https://doi.org/10.1029/2019GL084237.

Horner, T.J., Crockford, P.W., 2021. Barium isotopes in barite: drivers, dependencies, and distributions through space and time Geochemical Tracers in Earth System Science. In: Geochemical Tracers in Earth System Science, pp. 1–29.

Horner, T.J., Kinsley, C.W., Nielsen, S.G., 2015. Barium-isotopic fractionation in seawater mediated by barite cycling and oceanic circulation. Earth Planet. Sci. Lett. 430, 511–522. https://doi.org/10.1016/j.epsl.2015.07.027.

Horner, T.J., Pryer, H., Nielsen, S.G., Crockford, P.W., Gauglitz, J.M., Wing, B.A., Ricketts, R.D., 2017. Pelagic barite precipitation at micromolar ambient sulfate. Nat. Commun. 8 https://doi.org/10.1038/s41467-017-01229-5.

Hsieh, Y., Henderson, G.M., 2017. Barium stable isotopes in the global ocean: Tracer of Ba inputs and utilization. Earth Planet. Sci. Lett. 473, 269–278. https://doi.org/10.1016/j.epsl.2017.06.024.

Hsieh, Y., Bridgestock, L., Scheuermann, P.P., Seyfried, W.E., Henderson, G.M., 2021. Barium isotopes in mid-ocean ridge hydrothermal vent fluids: a source of isotopically heavy Ba to the ocean. Geochim. Cosmochim. Acta 292, 348–363. https://doi.org/10.1016/j.gca.2020.09.037.

Hu, Y., Luo, M., Liang, Q., Chen, L., Feng, D., Yang, S., Liang, J., Chen, D., 2019. Pore fluid compositions and inferred fluid flow patterns at the Haima cold seeps of the South China Sea. Mar. Pet. Geol. 103, 29–40. https://doi.org/10.1016/j.marpetgeo.2019.01.007.

Johnson, C.M., Beard, B.L., Albarède, F., 2004. Overview and General Concepts. Rev. Mineral. Geochem. 55, 1–24. https://doi.org/10.2138/gsrmg.55.1.1.

Kang, J., Bracco, J.N., Rimstidt, J.D., Zhu, G.H., Huang, F., Zhu, C., 2022. Ba attachment and detachment fluxes to and from barite surfaces in ^{137}Ba-enriched solutions with variable [Ba^{2+}]/[SO_4^{2-}] ratios near solubility equilibrium. Geochim. Cosmochim. Acta 317, 180–200. https://doi.org/10.1016/j.gca.2021.11.008.

Kiczka, M., Wiederhold, J.G., Frommer, J., Kraemer, S.M., Bourdon, B., Kretzschmar, R., 2010. Iron isotope fractionation during proton- and ligand-promoted dissolution of primary phyllosilicates. Geochim. Cosmochim. Acta 74, 3112–3128. https://doi.org/10.1016/j.gca.2010.02.018.

Lestini, L., Beaucaire, C., Vercouter, T., Descostes, M., 2013. Radium uptake by recrystallized gypsum: an incorporation study. Procedia Earth and Planetary Science 7, 479–482. https://doi.org/10.1016/j.proeps.2013.03.002.

Li, W., Beard, B.L., Johnson, C.M., 2011. Exchange and fractionation of Mg isotopes between epsomite and saturated $MgSO_4$ solution. Geochim. Cosmochim. Acta 75, 1814–1828. https://doi.org/10.1016/j.gca.2011.01.023.

Li, W., Kwon, K.D., Li, S., Beard, B.L., 2017. Potassium isotope fractionation between K-salts and saturated aqueous solutions at room temperature: Laboratory experiments and theoretical calculations. Geochim. Cosmochim. Acta 214, 1–13. https://doi.org/10.1016/j.gca.2017.07.037.

Li, W., Liu, X.M., Wang, K., Koefoed, P., 2021. Lithium and potassium isotope fractionation during silicate rock dissolution: an experimental approach. Chem. Geol. 568 https://doi.org/10.1016/j.chemgeo.2021.120142.

Ma, Z., Gray, E., Thomas, E., Murphy, B., Zachos, J., Paytan, A., 2014. Carbon sequestration during the palaeocene-eocene thermal maximum by an efficient biological pump. Nat. Geosci. 7, 382–388. https://doi.org/10.1038/ngeo2139.

Maher, K., Johnson, N.C., Jackson, A., Lammers, L.N., Torchinsky, A.B., Weaver, K.L., Bird, D.K., Brown, G.E., 2016. A spatially resolved surface kinetic model for forsterite dissolution. Geochim. Cosmochim. Acta 174, 313–334. https://doi.org/10.1016/j.gca.2015.11.019.

Matsuhisa, Y., Goldsmith, J.R., Clayton, R.N., 1978. Mechanisms of hydrothermal crystallization of quartz at 250°C and 15 kbar. Geochim. Cosmochim. Acta 42, 173–182.

McManus, J., Berelson, W.M., Klinkhammer, G.P., Johnson, K.S., Coale, K.H., Anderson, R.F., Kumar, N., Burdige, D.J., Hammond, D.E., Brumsack, H.J., Mccorkle, D.C., Rushdi, A., 1998. Geochemistry of barium in marine sediments: Implications for its use as a paleoproxy. Geochmica et Cosmochimica Acta 62, 3453–3473.

Monnin, C., Jeandel, C., Cattaldo, T., Dehairs, F., France, F., 1999. The marine barite saturation state of the world's oceans. Mar. Chem. 65, 253–261.

Oelkers, E.H., Pogge von Strandmann, P.A.E., Mavromatis, V., 2019. The rapid resetting of the Ca isotopic signatures of calcite at ambient temperature during its congruent dissolution, precipitation, and at equilibrium. Chem. Geol. 512, 1–10. https://doi.org/10.1016/j.chemgeo.2019.02.035.

Oelkers, E.H., Schott, J., 2001. An experimental study of enstatite dissolution rates as a function of pH, temperature, and aqueous Mg and Si concentration, and the mechanism of pyroxene/pyroxenoid dissolution. Geochim. Cosmochim. Acta 65, 1219–1231.

Oelkers, E.H., Benning, L.G., Lutz, S., Mavromatis, V., Pearce, C.R., Plümper, O., 2015. The efficient long-term inhibition of forsterite dissolution by common soil bacteria and fungi at Earth surface conditions. Geochim. Cosmochim. Acta 168, 222–235. https://doi.org/10.1016/j.gca.2015.06.004.

Oelkers, E.H., Berninger, U.-N., Pérez-Fernandez, A., Chmeleff, J., Mavromatis, V., 2018. The temporal evolution of magnesium isotope fractionation during hydromagnesite dissolution, precipitation, and at equilibrium. Geochim. Cosmochim. Acta 226, 36–49. https://doi.org/10.1016/j.gca.2017.11.004.

Parkhurst, D., Appelo, C., 2013. Description of Input and Examples for PHREEQC Version 3: A Computer Program for Speciation, Batch-Reaction, One-Dimensional Transport, and Inverse Geochemical Calculations. Denver, CO.

Paytan, A., Griffith, E.M., Eisenhauer, A., Hain, M.P., Wallmann, K., Ridgwell, A., 2021. A 35-million-year record of seawater stable Sr isotopes reveals a fluctuating global carbon cycle. Science 371 (6536), 1346–1350.

Paytan, A., Kastner, M., 1996. Benthic Ba fluxes in the central Equatorial Pacific, implications for the oceanic Ba cycle. Earth Planet. Sci. Lett. 142, 439–450.

Paytan, A., Kastner, M., Chavez, F.P., 1996a. Glacial to Interglacial Fluctuations in Productivity in the Equatorial Pacific as Indicated by Marine Barite. Science 1979 (22), 1355–1357.

Paytan, A., Kastner, M., Martin, E.E., Macdougall, J.D., Herbert, T., 1993. Marine barite as a recorder of strontium isotopes. Nature 366, 445–449.

Paytan, A., Moore, W.S., Kastner, M., 1996b. Sedimentation rate as determined by ^{226}Ra activity in marine barite. Geochim. Cosmochim. Acta 60, 4313–4319. https://doi.org/10.1016/S0016-7037(96)00267-0.

Pearce, C.R., Saldi, G.D., Schott, J., Oelkers, E.H., 2012. Isotopic fractionation during congruent dissolution, precipitation and at equilibrium: evidence from Mg isotopes. Geochim. Cosmochim. Acta 92, 170–183. https://doi.org/10.1016/j.gca.2012.05.045.

Rahman, S., Shiller, A.M., Anderson, R.F., Charette, M.A., Hayes, C.T., Gilbert, M., Grissom, K.R., Lam, P.J., Ohnemus, D.C., Pavia, F.J., Twining, B.S., Vivancos, S.M., 2022. Dissolved and Particulate Barium Distributions along the US GEOTRACES North Atlantic and East Pacific Zonal Transects (GA03 and GP16): Global Implications for the Marine Barium Cycle. Glob. Biogeochem. Cycles 36. https://doi.org/10.1029/2022GB007330.

Rees, C.E., 1973. A steady-state model for sulphur isotope fractionation in bacterial reduction processes. Geochim. et Cosmochim. Acta 37 (5), 1141–1162.

Rooze, J., Peterson, L., Peterson, R.N., Meile, C., 2020. Porewater flow patterns in surficial cold seep sediments inferred from conservative tracer profiles and early diagenetic modeling. Chem. Geol. 536 https://doi.org/10.1016/j.chemgeo.2020.119468.

Sauer, S., Hong, W.L., Yao, H., Lepland, A., Klug, M., Eichinger, F., Himmler, T., Crémière, A., Panieri, G., Schubert, C.J., Knies, J., 2021. Methane transport and sources in an Arctic deep-water cold seep offshore NW Svalbard (Vestnesa Ridge, 79°N). Deep Sea Res. 1 Oceanogr. Res. Pap. 167 https://doi.org/10.1016/j.dsr.2020.103430.

Schmitz, B., 1987. The Northward wandering of the Indian current. Paleoceanography 2, 63–77.

Schott, J., Oelkers, E.H., 1995. Dissolution and crystallization rates of silicate minerals as a function of chemical affinity. Pure & Applied Chemistry 67, 903–910.

Schott, J., Pokrovsky, O.S., Oelkers, E.H., 2009. The link between mineral dissolution/precipitation kinetics and solution chemistry. Rev. Mineral. Geochem. 70, 207–258. https://doi.org/10.2138/rmg.2009.70.6.

Siebert, C., Nägler, T.F., Kramers, J.D., 2001. Determination of molybdenum isotope fractionation by double-spike multicollector inductively coupled plasma mass spectrometry. Geochem. Geophys. Geosystems 2 (7).

Skulan, J.L., Beard, B.L., Johnson, C.M., 2002. Kinetic and equilibrium Fe isotope fractionation between aqueous Fe(III) and hematite. Geochim. Cosmochim. Acta 66, 2995–3015.

Smith, W., Chanley, M., 1975. Culture of Marine Invertebrate Animals, Culture of Marine Invertebrate Animals. Springer, US. https://doi.org/10.1007/978-1-4615-8714-9.

Snelgrove, S.H., Forster, C.B., 1996. Impact of seafloor sediment permability and thickness on off-axis hydrothermal circulation: Juan de Fuca Ridge eastern flank. Journal of Geophysical Research B: Solid Earth 101, 2915–2925. https://doi.org/10.1029/95jb03115.

Steefel, C.I., Druhan, J.L., Maher, K., 2014. Modeling coupled Chemical and Isotopic Equilibration rates. Procedia Earth and Planetary Science 10, 208–217. https://doi.org/10.1016/j.proeps.2014.08.022.

Tian, L.L., Zeng, Z., Nan, X.Y., Yu, H.M., Huang, F., 2019. Determining Ba isotopes of barite using the Na_2CO_3 exchange reaction and double-spike method by MC-ICP-MS. J. Anal. At. Spectrom. 34, 1459–1467. https://doi.org/10.1039/c9ja00064j.

Torapava, N., Ramebäck, H., Curti, E., Lagerkvist, P., Ekberg, C., 2014. Recrystallization of ^{223}Ra with barium sulfate. J. Radioanal. Nucl. Chem. 301, 545–553. https://doi.org/10.1007/s10967-014-3170-6.

van Zuilen, K., Müller, T., Nägler, T.F., Dietzel, M., Küsters, T., 2016a. Experimental determination of barium isotope fractionation during diffusion and adsorption processes at low temperatures. Geochim. Cosmochim. Acta 186, 226–241. https://doi.org/10.1016/j.gca.2016.04.049.

van Zuilen, K., Nägler, T.F., Bullen, T.D., 2016b. Barium Isotopic Compositions of Geological Reference Materials. Geostand. Geoanal. Res. 40, 543–558. https://doi.org/10.1111/ggr.12122.

Vinograd, V.L., Brandt, F., Rozov, K., Klinkenberg, M., Refson, K., Winkler, B., Bosbach, D., 2013. Solid-aqueous equilibrium in the $BaSO_4$-$RaSO_4$-H_2O system: First-principles calculations and a thermodynamic assessment. Geochim. Cosmochim. Acta 122, 398–417. https://doi.org/10.1016/j.gca.2013.08.028.

Vital, M., Daval, D., Morvan, G., Martinez, D.E., Heap, M.J., 2020. Barite Growth rates as a Function of Crystallographic Orientation, Temperature, and solution Saturation State. Cryst. Growth Des. 20, 3663–3672. https://doi.org/10.1021/acs.cgd.9b01506.

von Allmen, K., Böttcher, M.E., Samankassou, E., Nägler, T.F., 2010. Barium isotope fractionation in the global barium cycle: first evidence from barium minerals and precipitation experiments. Chem. Geol. 277, 70–77. https://doi.org/10.1016/j.chemgeo.2010.07.011.

Wiederhold, J.G., Kraemer, S.M., Teutsch, N., Borer, P.M., Halliday, A.N., Kretzschmar, R., 2006. Iron isotope fractionation during proton-promoted, ligand-controlled, and reductive dissolution of goethite. Environ. Sci. Technol. 40, 3787–3793. https://doi.org/10.1021/es052228y.

Zhen-Wu, B.Y., Dideriksen, K., Olsson, J., Raahauge, P.J., Stipp, S.L.S., Oelkers, E.H., 2016. Experimental determination of barite dissolution and precipitation rates as a function of temperature and aqueous fluid composition. Geochim. Cosmochim. Acta 194, 193–210. https://doi.org/10.1016/j.gca.2016.08.041.